COMPARATIVE ANALYSIS OF OSEM PARAMETERS FOR CARDIAC SPECT IMAGING ACROSS MULTIPLE CAMERA BRANDS: A MONTE CARLO STUDY

by

Ghassan Abojayab

B.S., in Biomedical Engineering, Bahcesehir University, 2022

Submitted to the Institute of Biomedical Engineering
in partial fulfillment of the requirements
for the degree of
Master of Science
in
Biomedical Engineering

Boğaziçi University
2024

COMPARATIVE ANALYSIS OF OSEM PARAMETERS FOR CARDIAC SPECT IMAGING ACROSS MULTIPLE CAMERA BRANDS: A MONTE CARLO STUDY

APPROVED BY:

Prof. Dr. Albert Güveniş ..... (Thesis Advisor)

Prof. Dr. Cengizhan Öztürk .....

Prof. Dr. Mehmet Kocatürk .....

DATE OF APPROVAL: 14 August 2024

ACKNOWLEDGMENTS

I would like to acknowledge and thank Professor Albert Guvenis for his invaluable assistance and resources in the development of this thesis. I am also deeply grateful to Professor Paul Segars of Duke University for generously providing me with a free license for the XCAT phantom program.

ACADEMIC ETHICS AND INTEGRITY STATEMENT

I, Ghassan Abojayab, hereby certify that I am aware of the Academic Ethics and Integrity Policy issued by the Council of Higher Education (YÖK) and I fully acknowledge all the consequences due to its violation by plagiarism or any other way.

Name :

Signature:

Date:

ABSTRACT

COMPARATIVE ANALYSIS OF OSEM PARAMETERS FOR CARDIAC SPECT IMAGING ACROSS MULTIPLE CAMERA BRANDS: A MONTE CARLO STUDY

To examine the effect of ordered subset expectation maximization (OSEM) parameters on the quantitative image quality of cardiac SPECT images in two different frequently used SPECT cameras and determine the optimal settings for producing images of best diagnostic quality. Another objective was to assess if different cameras produced a significant change in optimal parameters and levels of detectability. The optimization of OSEM iterative reconstruction algorithm was carried out by comparing image quality metrics, namely, contrast-to-noise ratio (CNR) and defect contrast across 12 OSEM subset-iteration combinations to find the best choice for cardiac perfusion SPECT images. Eight frames were reconstructed using the SIMIND Monte Carlo Simulation package. An activity of 370 MBq (10mCi) and projection acquisition interval of 20 seconds per projection were used. Attenuation (AC) and scatter corrections (SC) were performed in this study for all images. The 16-2 subset-iteration combination yielded the highest CNR and defect contrast values for both cameras. The difference between CNR values for two cameras was found to be around 5% only. Monte Carlo simulations can be useful to investigate how quantitative image quality behaves with respect to reconstruction parameters and correction algorithms in a controlled environment. The found optimum is similar to values reported in previous findings. In this study, the use of different camera brands did not affect the optimum. The quantitative detectability measures were also very similar.

Keywords: Myocardial Perfusion Imaging; Single Photon Emission Computed Tomography; Contrast-to-noise ratio; SNR; Monte Carlo; SIMIND.

ÖZET

TEZİN TÜRKÇE BAŞLIĞI

İki farklı sıkça kullanılan SPECT kamerada sıralı alt kümeler beklenti maksimizasyonu (OSEM) parametrelerinin kardiyak SPECT görüntülerinin kantitatif görüntü kalitesine etkisini incelemek ve en iyi tanısal kalitede görüntüler üretmek için optimal ayarları belirlemek. Diğer bir amaç ise farklı kameraların optimal parametrelerde ve tespit edilebilirlik seviyelerinde önemli bir değişiklik yapıp yapmadığını değerlendirmek. OSEM iteratif rekonstrüksiyon algoritmasının optimizasyonu, 12 OSEM alt küme-iterasyon kombinasyonunda kontrast-gürültü oranı (CNR) ve defekt kontrastı gibi görüntü kalitesi metriklerini karılatırarak gerçekleştirildi. Sekiz çerçeve SIMIND Monte Carlo Simülasyon paketi kullanılarak yeniden oluşturuldu. 370 MBq (10mCi) aktivite ve her projeksiyon için 20 saniyelik projeksiyon edinim aralığı kullanıldı. Bu çalımada tüm görüntüler için attenuasyon (AC) ve saçılma düzeltmeleri (SC) yapıldı. 16-2 alt küme-iterasyon kombinasyonu, her iki kamera için en yüksek CNR ve defekt kontrastı değerlerini verdi. İki kamera için CNR değerleri arasındaki fark yalnızca %5 civarında bulundu. Monte Carlo simülasyonları, rekonstrüksiyon parametreleri ve düzeltme algoritmalarına ilişkin kantitatif görüntü kalitesinin nasıl davrandığını kontrol edilen bir ortamda aratırmak için yararlı olabilir. Bulunan optimum, önceki bulgularda bildirilen değerlere benzer. Bu çalımada, farklı kamera markalarının kullanımı optimumu etkilemedi. Kantitatif tespit edilebilirlik ölçütleri de çok benzerdi.

Keywords: Myocardial Perfusion Imaging; Single Photon Emission Computed Tomography; Contrast-to-noise ratio; SNR; Monte Carlo; SIMIND.

TABLE OF CONTENTS

ACKNOWLEDGMENTS iii
ACADEMIC ETHICS AND INTEGRITY STATEMENT iv
ABSTRACT v
ÖZET vi
LIST OF FIGURES ix
LIST OF TABLES xi
LIST OF SYMBOLS xii
LIST OF ABBREVIATIONS xiii
1. INTRODUCTION 1
1.1 Literature Review 3
1.2 Study Problem 6
1.3 Study Aim 6
1.4 Limitations 7
1.5 Study Outline 7
2. BACKGROUND 9
2.1 SPECT Instrumentation and Acquisition 9
2.1.1 Gamma Camera Resolution 12
2.2 Cardiac Imaging 13
2.3 Photon Interactions 14
2.3.1 Compton Scattering 14
2.3.2 The Photoelectric Effect 16
2.3.3 High-Energy Photons Attenuation 17
2.4 Types of Corrections 18
2.4.1 Attenuation Correction 18
2.4.2 Scatter Correction 19
2.5 Reconstruction Methods 21
2.5.1 Analytical (FBP) Reconstruction 21
2.5.2 Iterative Reconstruction (IR) 24
2.6 Ordered Subsets Expectation Maximization Algorithm 25

2.7 Monte Carlo (MC) Simulation in Medical Imaging 26
2.7.1 Distribution function method 27
2.7.2 The "rejection" method 28
3. METHODS 29
3.1 The Extended Cardiac-Torso (XCAT) Phantom 29
3.1.1 Generation of Normal and Defective Phantoms 29
3.1.2 Activity Distribution 30
3.2 SIMIND Monte Carlo Simulation 31
3.2.1 Simulation and Acquisition 32
3.2.2 Reconstruction and Corrections 32
3.3 Filtering 33
3.4 Image Quality Assessment 34
4. RESULTS 36
4.1 Statistical Analysis 37
5. CONCLUSION 39
5.1 Findings 39
5.2 Clinical Significance 39
5.3 Comparison to literature 40
5.4 Future work and limitations 40
APPENDIX A. SIMIND SIMULATIONS 42
A.1 Simulating the 1st Frame using Camera 1 42
A.1.1 Reconstruction Run for 16-2 Parameter 45
A.2 Simulating the 1st Frame using Camera 2 46
A.2.1 Reconstruction Run for 16-2 Parameter 49
APPENDIX B. XCAT PHANTOM PROGRAM 52
REFERENCES 56

LIST OF FIGURES

Figure 1.1	Essential five steps for any ET study [1].	2
Figure 1.2	Detection Performance (AUC) of OSEM with AC, SC, and RC vs FBP at different cutoff frequencies [2].	4
Figure 2.1	Types of collimators used in cardiac SPECT [1].	10
Figure 2.2	Diagram of a typical SPECT gamma camera: Collimator images the patient on a scintillation crystal, converting gamma rays to light, detected by photomultiplier tubes, with a computer processing and displaying the resulting images [1].	11
Figure 2.3	Diagram of the arrangement of PMTs and their internal components [1].	12
Figure 2.4	Illustration of the Compton scatter process involving outer-shell electrons in the plane [1].	15
Figure 2.5	Final photon energy as a function of scattering angle for incident photon energies of 140 keV and 511 keV [1].	16
Figure 2.6	Illustration of the photoelectric effect with a more probable involvement of the inner-shell electrons in the plane [1].	17
Figure 2.7	(A) Demonstration of the energy windows employed in the Dual-energy window correction method superimposed on the 99mTc energy spectrum [3]. (B) Depiction of the TEW correction method's spectral representation utilizing trapezoidal approximation [4].	20
Figure 2.8	First, (a) photons are emitted in parallel directions, pass through the collimator, and form a projection image. The camera is then rotated to capture a different perspective of the same distribution. Next, (b) the acquired data is rearranged into a sinogram. Finally, (c) the data is back-projected into the object domain to produce an estimated activity distribution [5].	22
Figure 2.9	Blurring caused by FBP [6].	22
Figure 2.10	Steps of reconstruction of an object by FBP [5].	25

Figure 3.1 Steps of creating a defective phantom. Part A is the normal healthy phantom, part B shows the defect on its own, and part C is the result after subtraction of part B from A. 30

Figure 3.2 The difference in image quality after applying the butterworth filter with an order of 3 and cutoff frequency of 0.5. 34

Figure 3.3 ROI selection using the Phantom file as a template. Part A shows the XCAT phantom file for frame 6 with the healthy LV ROI drawn in orange and part B shows the reconstructed image of the same frame with the same ROI overlayed. 35

Figure 4.1 SPECT images obtained using Camera 1 and Camera 2 with different OSEM parameters 36

Figure 4.2 The defect contrast, CNR, and SNR values across the OSEM parameters. The first row shows those values with Poisson noise included, while the 2nd row shows the results without Poisson noise. 37

LIST OF TABLES

Table 3.1	Measurements of the 50th percentile male phantom [7].	30
Table 3.2	Relative Uptake Ratios in the XCAT phantom from 99mTc-MIBI	31
Table 3.3	Comparison of Camera 1 and Camera 2 Parameters	31
Table 3.4	Specifications of the SPECT/CT systems used.	32
Table 3.5	Energy Windows and their Widths	33
Table 4.1	Comparison of Defect Contrast, CNR, and SNR between Camera 1 (C1) and Camera 2 (C2).	38

LIST OF SYMBOLS

a_{ij}	Description of a_{ij}
α	Description of α

LIST OF ABBREVIATIONS

SPECT	Single Photon Emission Computered Tomography
OSEM	Ordered Subsets Expected Maximization
MPI	Myocardial Perfusion Imaging
FBP	Filtered Backprojection
LEHR	Low-Energy High-Resolution
XCAT	Extended Cardiac-Torso
^{99m}Tc	The radioactive isomer of Technetium-99
SIMIND	Simulating Medical Imaging Nuclear Detectors

1. INTRODUCTION

Emission tomography (ET) is a subfield of medical imaging encompassing two primary methods - single-photon emission computed tomography (SPECT) and positron emission tomography (PET) [1]. These techniques employ radioactive substances to visualize various physiological aspects of the body. ET is valuable for detecting tumors, pinpointing regions of the heart impacted by coronary artery disease, and identifying brain areas influenced by drugs [1]. As the term "emission tomography" implies, this imaging approach combines two fundamental concepts: utilizing gamma-ray emission (known as the tracer principle) and creating three-dimensional internal body images (referred to as tomography) [1]. PET and SPECT primarily differ in the radioisotopes they use as tracers. In SPECT studies, radiopharmaceuticals are labeled with single-photon emitters, which release one gamma-ray photon per radioactive decay event [1]. One example of this kind of radiotracers is Technetium-99m, usually used for myocardial perfusion imaging (MPI), which is a firmly established, noninvasive imaging method extensively applied for assessing individuals with either a confirmed or suspected coronary artery disease (CAD) [8]. Numerous investigations have substantiated the robust diagnostic and prognostic utility of SPECT MPI. Gated SPECT MPI offers precise insights into both the distribution of the tracer across myocardial walls and the functioning of the left ventricle in a single comprehensive diagnostic examination [8].

According to the World Health Organization, ischemic heart disease emerged as the leading cause of deaths, accounting for 16% of the total mortality. Since the year 2000, it has exhibited the most substantial surge in death rates, with an increase of over 2 million deaths, reaching nearly 9 million deaths by 2019 [9]. Fortunately, such diseases can be diagnosed by performing myocardial perfusion imaging (MPI) using SPECT and other imaging modalities. The significance of MPI in the context of ischemic heart disease lies in its ability to noninvasively assess myocardial perfusion and diagnose CAD, which is crucial in understanding the widespread impact of ischemic heart disease, especially in the context of coronary artery blockages.

The two primary methods that are utilized for visualizing the distribution of radiotracers in emission tomography (ET) are projection imaging and tomography. To put it simply, a projection image is akin to what an external observer would see when looking through the body from the outside. In contrast, a tomographic image represents a cross-sectional slice of the body, with "tomography" originating from Greek words signifying "slice" and "drawing." The remarkable aspect of tomography lies in its capacity to provide us with an internal view of the body from this unique perspective, all without the need of surgical intervention. The data captured by the imaging equipment are obtained in the form of projections. Tomographic images, however, cannot be directly observed; they are instead computed by a computer using the projection measurements in a process known as image reconstruction, a topic that will be discussed thoroughly in this study [1].

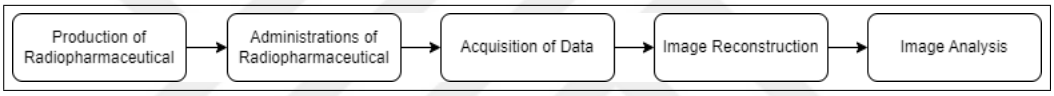


Figure 1.1 Essential five steps for any ET study [1].

In order to obtain a cardiac perfusion image of diagnostic quality, different corrections and reconstruction techniques are utilized. SPECT images can be reconstructed using either the analytical filtered back projection (FBP) method or iteratively through algebraic approaches [10]. The importance of these methods is in converting raw data into meaningful clinical images [10]. Lately, iterative reconstruction (IR) of images, specifically through ordered subsets expectation maximization (OSEM) algorithm is the most commonly used reconstruction algorithm in clinical practice. Due to its iterative nature and computational superiority over other reconstruction techniques like conventional FBP, OSEM has helped in creating higher quality images in shorter durations [11],[2],[12].

Transition paragraph to Monte carlo by mentioning osem optimization via simulation.

Monte Carlo numerical simulation methods, named after the famous casino in Monte Carlo and their reliance on random numbers, are statistical techniques used

for simulating specific scenarios. These simulations involve modeling the system and physical processes using known probability density functions (pdfs) to enable random sampling. Performing a large number of simulations is essential for obtaining accurate parameter estimates [13]. Simulation studies offer numerous advantages over experimental studies. They provide flexibility in altering parameters and assessing their impact on system performance. Additionally, they allow the investigation of parameters that are difficult or impossible to measure experimentally, such as the scatter component in radiation emissions. Monte Carlo simulations, incorporating known physics, can mimic scatter events and their impact on the final image. This approach aids in understanding complex processes, as it provides access to all simulation details [13].

1.1 Literature Review

There has been multiple works that discussed iterative reconstruction in cardiac SPECT and the effect of optimizing the OSEM algorithm parameters in the aim of maximizing the image quality and quantitative metrics. The difference in image quality as a result of using different correction types with OSEM was examined in multiple studies [2],[14]. Additionally, other studies have investigated and evaluated different combinations of subsets and iterations for OSEM [15],[16].

In nearly all the reviewed papers, OSEM consistently demonstrated superior image quality compared to FBP. For instance, a study by A. J. Ramon et al. [2] emphasized the superior performance of OSEM reconstruction, especially when integrated with attenuation correction (AC), scatter correction (SC), and depth-dependent resolution recovery (RR). This combination not only maintained image quality but also enabled a reduction in the administered dose while still achieving images of equivalent quality to those obtained with FBP. This section will dive deeper into the different outcomes that have been found in the literature regarding this topic.

In study [2], the aim was to assess the potential reduction in administered dose without compromising diagnostic accuracy across three reconstruction strategies uti-

lized in cardiac SPECT imaging. The optimized strategies included FBP and OSEM with various corrections. In the case of FBP, the optimal values for the area under the receiver operating characteristic curve (ROC) curve at different dose levels were 0.75, 0.74, 0.72, and 0.70 for 100%, 50%, 25%, and 12.5% of the standard dose, respectively. Conversely, for OSEM with attenuation correction (AC), scatter correction (SC), and resolution correction (RC), the corresponding values were 0.81, 0.79, 0.76, and 0.74. For OSEM with SC and RC, the values were 0.78, 0.77, 0.74, and 0.72. Those findings suggest that reconstructions performed by OSEM with AC, SC, and RC could potentially be reduced, on average, to 25% of the original dose without diminishing diagnostic accuracy below that achieved with FBP.

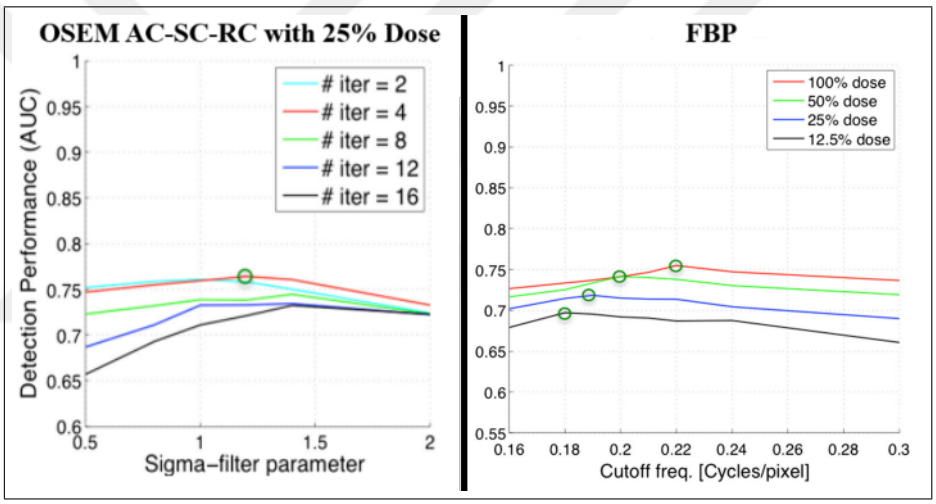


Figure 1.2 Detection Performance (AUC) of OSEM with AC, SC, and RC vs FBP at different cutoff frequencies [2].

In another study, Okuda et al. [14] aimed to define the optimal reconstruction parameters for OSEM by utilizing an identical combination of corrections alongside OSEM reconstruction, including attenuation correction, scatter correction, and depth-dependent resolution recovery. The study involved evaluating these optimal parameters in an anthropomorphic torso phantom study and assessing their applicability in both normal volunteer and abnormal perfusion patient groups. The assessment included calculating the normalized mean square error (NMSE) for phantom images to determine the optimal OSEM update and the full width at half maximum (FWHM) of the Gaussian filter. Validation of myocardial count, contrast, and noise characteristics for clinical subjects from OSEM_{ACSCRR} processing was conducted. Comparisons were

made with simultaneous OSEM with depth-dependent resolution recovery ($OSEM_{RR}$) and FBP performances. Results indicated that applying $OSEM_{ACSCRR}$ with 90−120 OSEM updates and a Gaussian filter with 13.2−14.85 mm FWHM resulted in a low NMSE value in the phantom study. Notably, using $OSEM_{ACSCRR}$ with 120 updates and a Gaussian filter with 13.2 mm FWHM in normal volunteers showed significantly higher myocardial contrast compared to 120 updates and 14.85 mm FWHM. $OSEM_{ACSCRR}$ with 90−120 OSEM updates and 14.85 mm FWHM produced the lowest root mean square (RMS) noise. The study concluded that the clinically optimized parameters for OSEM updates and FWHM of the Gaussian filter were (1) 120 updates and 13.2 mm and (2) 90−120 updates and 14.85 mm on the $OSEM_{ACSCRR}$ processing, respectively. The study also highlighted the need for further investigation of optimal OSEM reconstruction parameters in low-count acquisition and the evaluation of myocardial count, contrast, and noise characteristics in a larger patient population [14].

Dheer et al. [15], on the other hand, aimed to determine the most suitable parameters for OSEM in the reconstruction of images obtained from Tc-99m MIBI myocardial perfusion SPECT. The study involved a retrospective analysis of 99 stressârest Myocardial Perfusion SPECT studies, utilizing 16 different combinations of iterations and subsets for image reconstruction through both OSEM and FBP methods. The optimal iterationâsubset combination, providing the highest visual quality images, was identified for each patient and subsequently compared with FBP-reconstructed images. Results indicated that the most favorable image quality was achieved using a combination of four iterations and six subsets for both cases, with and without a Butterworth filter. Substantial interobserver agreement was observed for OSEM images; however, upon comparison, FBP images exhibited superior quality than OSEM-reconstructed images without a Butterworth filter. The research explored the correlation of cardiac function parameters between FBP and OSEM methods, highlighting their limitations. The conclusion suggested a robust correlation between parameters derived from FBP and OSEM construction methods, notwithstanding potential significant differences. The retrospective nature and the need of a larger population were limiting factors in this study [15].

1.2 Study Problem

It is possible that the optimal OSEM parameters could change for different brands due to several factors such as resolution and sensitivity or the design of the collimator, and the specific implementation of the OSEM algorithm by each manufacturer. Different camera brands utilize varying sensor technologies, resulting in different levels of image noise, which influences the optimal number of iterations needed to achieve the desired noise reduction. Similarly, variations in camera sensor resolutions mean that higher resolution images may require more iterations for comparable noise reduction. Additionally, while the core principles of OSEM remain consistent, the specific implementation by each manufacturer can differ, affecting the necessary number of iterations for optimal performance. Therefore, a simulation study investigating the optimal number of OSEM iterations for different SPECT camera brands would be useful.

Within SPECT imaging guidelines, specific reconstruction parameters are often outlined for filtered back projection (FBP), including details such as cut-off frequencies and filter orders tailored for rest and stress studies [15]. In instances where these parameters are not explicitly addressed in the guidelines, vendors may typically provide them. However, it's important to note that optimal OSEM reconstruction parameters are usually not indicated in the guidelines. This gap serves as the impetus for this study, which seeks to establish and optimize these parameters in hopes of establishing the optimal use of OSEM algorithm in MPI SPECT studies and find the answer to the question of how these values change according to the type of SPECT camera used.

1.3 Study Aim

The study aims to optimize the OSEM algorithm for SPECT cardiac perfusion imaging and examine the effect of different combinations of subsets and iterations on quantitative metrics such as the defect contrast percentage CNR. By using Simulating Medical Imaging Nuclear Detectors (SIMIND) Monte Carlo software to simulate two

different SPECT systems, in conjunction with the XCAT phantom program to create normal and defective phantoms, the research seeks to define the best OSEM parameters for each of the cameras, thereby improving image quality and clinical utility. The study aims to enhance OSEM's role in cardiac imaging, leading to more accurate diagnoses and improved patient care.

1.4 Limitations

It is important to note that the study is limited for its reliance on simulation environments, which are valuable but may not fully represent the complexities of real-world clinical settings. Moreover, only a male phantom was considered in this study, which leaves a space for uncertainty in the results when the patient is a female. Moreover, the computational power and time needed for optimizing OSEM, particularly concerning reconstruction with different pairs of subsets and iterations, should be noted. The study primarily explores the effects of different subsets and iterations within a specific parameter range, possibly leaving out various clinical scenarios. Therefore, clinical validation may be required to determine the practical applicability of the study's findings.

1.5 Study Outline

To be as thorough as possible, chapter two provides background information on medical imaging, with a focus on Single Photon Emission Computed Tomography (SPECT) cardiac imaging and related reconstruction techniques, as well as the critical role Monte Carlo (MC) simulation plays in medical imaging. A comprehensive overview of the most recent research on OSEM optimisation is presented in Chapter 3. It highlights how crucial it is to optimise the OSEM algorithm in light of SPECT imaging and how doing so could improve diagnostic precision. The examination of earlier research on OSEM optimisation throws light on the difficulties that have been

encountered. In Chapter 4, the Extended Cardiac-Torso (XCAT) Phantom is presented and its function in producing attenuation and normal activity maps along with perfusion deficiencies is explained. In addition, it describes the process for Monte Carlo simulation of cardiac SPECT, including the simulation programme and the simulation of 99mTc-labeled Tetrofosmin in two distinct SPECT systems. Eventually, a thorough explanation of the study's conclusions and findings is given in the chapters on the results and conclusion.

2. BACKGROUND

2.1 SPECT Instrumentation and Acquisition

The SPECT imaging process begins with the administration of a radiopharmaceutical, typically through injection [1]. Subsequently, the imaging equipment detects and records gamma rays emitted by the radiotracer due to radioactive decay [1]. Because there are safety constraints on the dose of radiopharmaceutical that can be administered to a patient, the gamma-ray emissions rate is relatively low, usually around 10^4 counts per second per milliliter of the desired tissue in a SPECT study [1]. Hence, a SPECT study necessitates a relatively extended data collection period [1].

SPECT employs a collimator, composed of a dense material like lead, perforated with a honeycomb-like structure of long, narrow channels [1]. This collimator selectively captures rays traveling in a specific direction, corresponding to the orientation of its channels. Gamma rays moving in different directions are either obstructed by the channel walls or completely bypass the collimator [1]. Commercially, there are three collimator varieties employed in cardiac SPECT: the parallel-hole, the cardio-focal, and the pinhole collimators (Figure 2.1) [17]. They also come in various designs and hole shapes. Holes of hexagonal shape are the most commonly used due to their general efficiency. While most collimators feature parallel holes, some have bore patterns that either converge or diverge. Converging collimators have the ability to magnify an image on the camera face, potentially resulting in finer resolution and higher sensitivity images, especially when imaging small objects relative to the detector face, compared to parallel-hole collimators [1]. In this study, parallel hole collimators with the hexagonal configuration are utilized. Additionally, there are four main types of parallel-hole collimators used in nuclear medicine, each designed for specific energy ranges and corresponding radioisotopes. These types are LEHR (low-energy, high-resolution), LEAP (low-energy, all-purpose), MEAP (medium-energy, all-purpose), and HEAP (high-energy, all-purpose). The designations indicate the energy range they are

suitable for accommodating radioisotopes like 57Co, 123I, ^{99m}Tc, 201Tl for LE collimators, 67Ga and 111In for ME collimators, and 131I for HE collimators. The choice of collimator type involves a trade-off between resolution and sensitivity, influenced by factors such as septal material, bore diameter, bore length, and septal thickness [1].

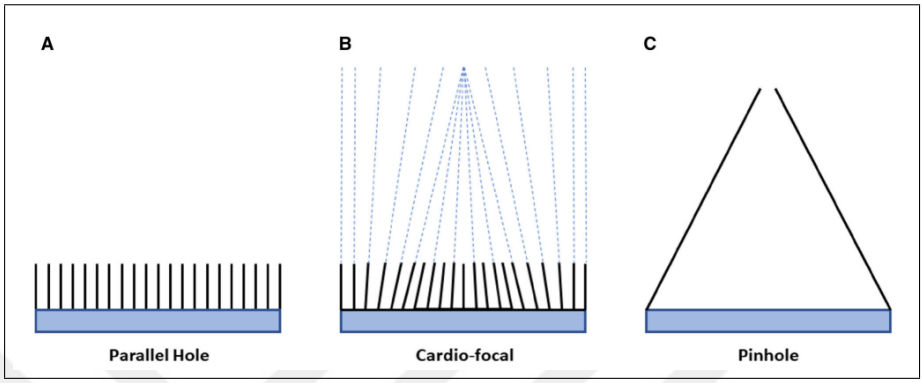


Figure 2.1 Types of collimators used in cardiac SPECT [1].

After the gamma photons pass through the collimator, the unabsorbed photons encounter the gamma camera, also known as an Anger camera, with detection hardware located on the side opposite the collimator from the subject. A gamma photon that passes successfully through the collimator hits the initial component of the detection system, a scintillator crystal, which transforms the high-energy gamma photon into numerous visible light photons. These photons are subsequently detected by a series of photomultiplier tubes (PMTs), which operate based on the photoelectric effect. Each PMT consists of a photocathode, 6-10 dynodes, and an anode. During PMT operation, distinct voltage variations are maintained between its dynode stages, photocathode, and anode. A PMT can generate a cascade of electrons from a single photoelectron, resulting in a detectable electrical current. This current is captured by associated electronic components that record when an event occurs [1]. These processes are simplified in schematic diagram in Figure 2.2 and 2.3 .

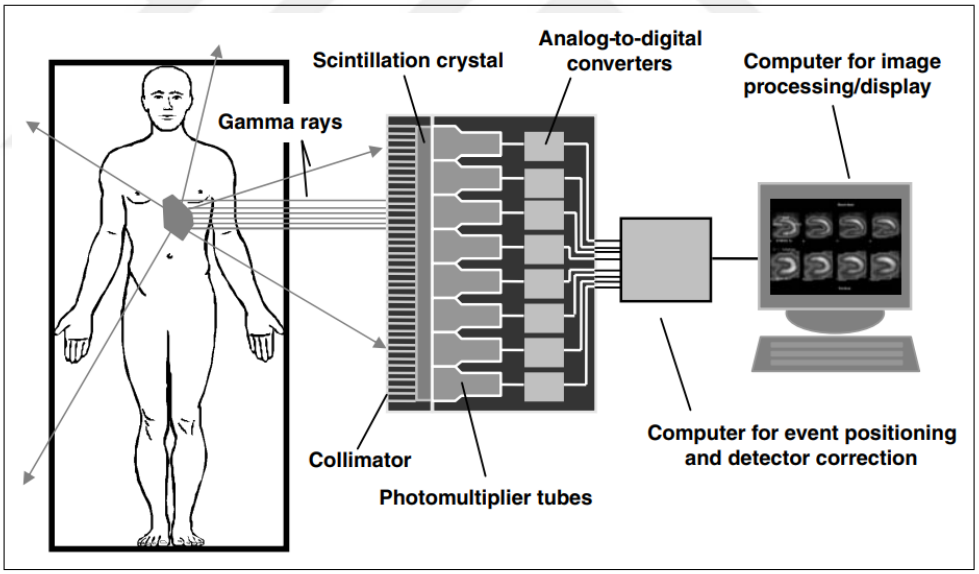


Figure 2.2 Diagram of a typical SPECT gamma camera: Collimator images the patient on a scintillation crystal, converting gamma rays to light, detected by photomultiplier tubes, with a computer processing and displaying the resulting images [1].

Once the gamma rays (events) are captured and converted to electrical signals, they go through event positioning and detector correction before being processed and reconstructed into helpful diagnostic images via the preferred method of image reconstruction. There are three key factors that influence image reconstruction which must be considered: photon attenuation, scattering and depth-dependent blur. The

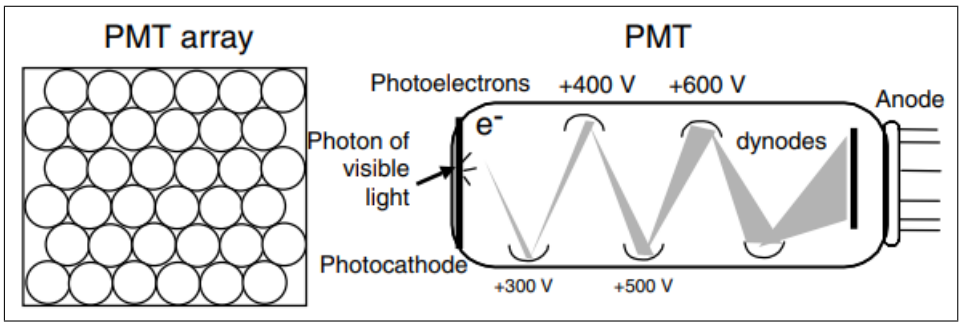


Figure 2.3 Diagram of the arrangement of PMTs and their internal components [1].

attenuation of gamma rays is inevitable, especially when emitted from deep within the object, causing a depth-dependent effect. If left unaccounted for, this attenuation can result in dark regions within the reconstructed image. Moreover, scatter interactions between the gamma photons and the body of the patient materials can cause radiation to deviate from its initial path. This leads to a non-linear blurring effect in the image, potentially distorting the information. Unlike an ideal scenario where collimator channels would be infinitely narrow, real collimators have finite spatial extents and capture a cone-looking region of radiation emanating from the channel. This creates depth-dependent blurring in the image, with the most significant impact on regions of the object located farthest from the collimator [1].

2.1.1 Gamma Camera Resolution

Usually measured as the full width at half-maximum (FWHM) or full width at tenth-maximum (FWTM), the intrinsic spatial resolution of a gamma camera represents the detector's resolution limit, assuming perfect collimation. The spatial resolution of the entire camera system, including collimator and position-sensitive detector, is a combined outcome of collimator and intrinsic resolutions. Intrinsic resolution is influenced by various factors, such as the Poisson process noise in scintillation photon production, finite energy resolution of the scintillation crystal due to compositional variations, finite energy resolution of photomultiplier tubes caused by fluctuations in photoelectron yield, variability in detector response due to photon-crystal interactions, and various scatterings of gamma photons within the crystal resulting in average en-

ergy deposits that are not consistent with the original interaction point. The primary factor that degrades the detector's intrinsic resolution in gamma cameras is Poisson noise during scintillation photon production. Photons with lower energy contribute to reduced intrinsic resolution as they generate lesser visible light photons, leading to a lower signal-to-noise ratio. Typically ranging from 3 to 5 mm, the intrinsic resolution depends on factors such as crystal thickness, the number of PMTs, and the algorithms used for position localization in the gamma camera detector [1].

Collimator resolution is determined by the collimator design. A longer bore length, with other factors held constant, results in finer resolution but reduced sensitivity. Conversely, a larger bore diameter, under constant conditions, leads to higher sensitivity but poorer resolution. Collimator resolution, which is influenced by the distance from the collimator surface, is typically defined at 10 cm from the collimator face and ranges from a few millimeters to a few centimeters, varying based on the design of the collimator. On the other hand, the energy resolution of a detector is influenced by the level of fluctuation in the outputs of photomultiplier tubes (PMTs) due to variations in the signal generation process initiated by a photon-crystal interaction. In contemporary gamma cameras using NaI(Tl)/PMT-array scintillation detectors, the energy resolution typically falls within the range of $9-11\%$. This parameter is crucial for image quality, as a finer energy resolution enhances the capability to reject scattered photons effectively [1].

2.2 Cardiac Imaging

In cardiac imaging, the components of the SPECT do not change however there are some variables that can be tuned for this kind of studies. Those variables include the collimator, matrix size, angular range, dose, and the radiotracer used. For myocardial perfusion imaging, an ideal radiotracer should offer high myocardial uptake without significant redistribution, maintain a stable target-to-background ratio with minimal uptake in the lungs, liver, stomach, and gut, exhibit rapid blood clearance, and establish a linear relationship between myocardial uptake and coronary blood flow [18]. As of

now, ^{99m}Tc-Sestamibi and ^{99m}Tc-Tetrofosmin stand as the predominant ^{99m}Tc-labeled radiopharmaceuticals employed in the investigation of ischemic heart disease [18].

In cardiac SPECT, a detailed three-dimensional representation of radioactive tracers injected into the patient is obtained, offering valuable insights into the functional behavior of the heart. Projection acquisition can be executed in three distinct manners: step-and-shoot, continuous, and continuous step-and-shoot. In the step-and-shoot method, which is the most commonly employed, the camera halts at predefined angular positions during the imaging orbit and captures projections for predetermined time intervals [10]. Typically, this method covers a 180-degree arc, spanning from 45 degrees right anterior oblique to left posterior oblique (RAO-LPO) [10]. Reconstruction algorithms are then used to compute a precise 3D distribution of radioactivity based on the gathered projections.

2.3 Photon Interactions

Due to their lack of electric charge, photons engage with molecules, atoms, electrons, and nuclei differently compared to beta particles, exhibiting a lower probability of interaction. However, the presence of an electromagnetic field in photons allows them to interact with electric charge. In the realm of nuclear medicine, where specific photon energies are of interest, interactions predominantly occur with individual atomic electrons. As energy is transferred to these electrons, the resulting charged particle traverses through matter. Notably, high-energy photons in this context primarily undergo two significant interactions with individual atomic electronsâthe Compton effect and the photoelectric effect [1].

2.3.1 Compton Scattering

If the energy and momentum of an incident photon significantly exceed the momentum and binding energy of an impacted electron, it is permissible, for calculation

purposes, to consider the electron as either roughly unbound (free) or loosely bound and stationary. Due to the conservation principles of energy and momentum and the mass differential between the massless photon and the non-negligible electron, a high-energy photon cannot be entirely absorbed by a stationary, loosely bound electron, necessitating the photon to scatter and undergo energy loss. This phenomenon, where a photon with high energy interacts with a free or loosely bound atomic electron, is referred to as Compton scattering. Figure 2.4 shows the initial and final velocity vectors of the photon and electron in the plane where the scattering takes place. In the medical energy range of photons, Compton scatter predominantly involves outer-atomic-shell electrons, given their more tenuous binding. Utilizing expressions such as $E_i = p_i c$ and $E_f = p_f c$ for photons, we can derive Eq. 2.1, representing the final photon energy concerning the initial photon energy, electron rest mass, and photon scatter angle [1].

$$E_f = \frac{E_i}{1 + \frac{h}{m_e c^2}(1 - \cos\theta)} \tag{2.1}$$

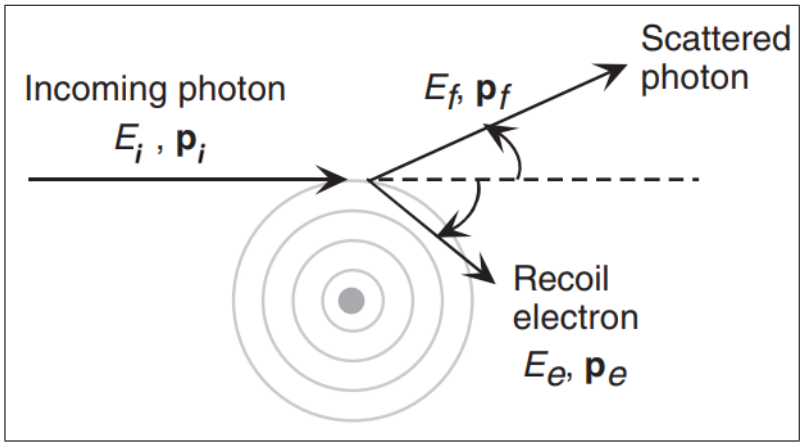


Figure 2.4 Illustration of the Compton scatter process involving outer-shell electrons in the plane [1].

In the case of electrons that are loosely bound, the energy of the recoil electron is determined by the gap between the energies of the initial and final photon, denoted as $E_i - E_f$. In the context of gamma-ray energies pertinent to nuclear medicine, the recoil electron is typically absorbed within a short distance, usually a few millimeters

or less, contingent upon the specific characteristics of the absorbing medium and the energy of the electron. The maximum energy of the recoil electron, denoted as T_{max}, occurs when the scattered photon has its lowest energy, particularly in situations where the photon undergoes backscattering ($\theta = 180°$ in Eq. 2.4) [1].

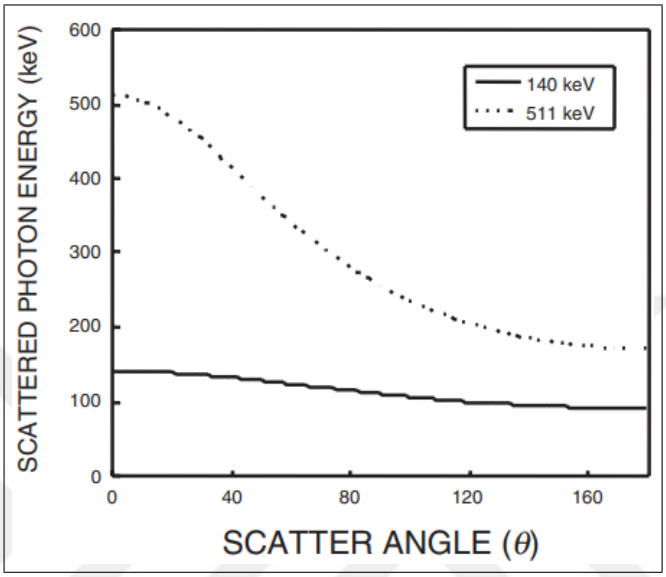


Figure 2.5 Final photon energy as a function of scattering angle for incident photon energies of 140 keV and 511 keV [1].

2.3.2 The Photoelectric Effect

Thee photoelectric effect is a process where a gamma ray can transfer its entire energy to a bound electron. In this process, the atom absorbs some of the recoil momentum, ensuring conservation of both energy and momentum. The ejected electron, referred to as a photoelectron, results from this interaction, and the incident photon ceases to exist. This phenomenon is illustrated in Figure 2.6. Because a free electron cannot completely absorb a photon, the photoelectric effect primarily involves bound electrons, especially those in the inner K shell, as well as in the three L subshells, five M subshells, or seven N subshells. The involvement of a third body, such as the nucleus, is essential for conserving momentum, which increases the likelihood of photoelectric absorption occurring with electrons that are tightly bound. As photon energies surpass the binding energy of the K shell, around 80% of photoelectric absorption events involve electrons in the K shell. For energies above the K-shell, absorbtion of all energies

is possible, resulting in a continuous absorption spectrum, while energies below the K-shell, most photoabsorption occurs with L and M electrons [1].

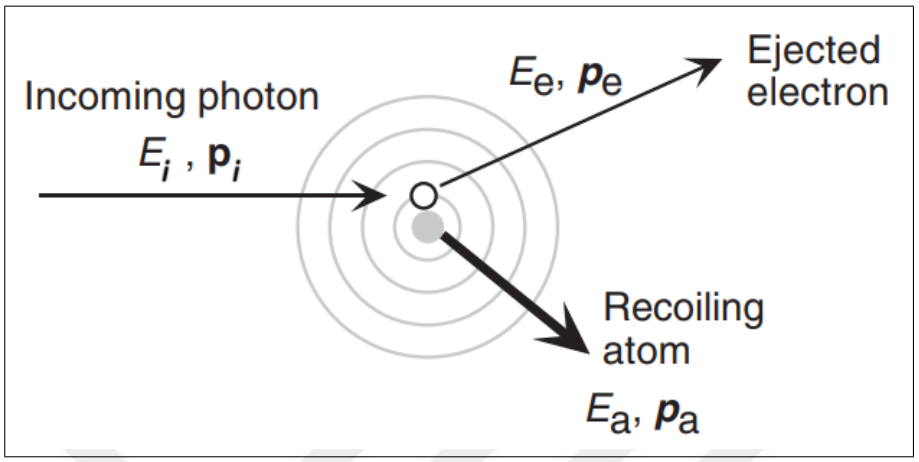


Figure 2.6 Illustration of the photoelectric effect with a more probable involvement of the inner-shell electrons in the plane [1].

Taking into account considerations of energy and momentum, the atom's recoil kinetic energy E_a is approximately $\frac{m_e}{M_a}E_e$, where M_a represents the atomic mass. Since the ratio $\frac{m_e}{M_a}$ is typically around 10^{-4}, E_a can be neglected. Consequently, conservation of energy implies the following for the kinetic energy of the electron, E_e [1]:

$$E_e = E_i - E_B \tag{2.2}$$

2.3.3 High-Energy Photons Attenuation

The interaction of gamma rays and annihilation photons with matter presents distinctive characteristics, with their heightened penetration capabilities attributed to smaller cross-sections in primary interaction processes such as Compton scatter and photoelectric absorption, contrasting them from charged particles like electrons. Unlike charged particles, a photon beam does not undergo energy degradation while passing through matter; instead, it experiences intensity attenuation due to interactions like Compton scatter and the photoelectric effect, which either scatter or absorb photons, removing them from the beam [1].

The unaltered photons that pass through the material retain their full energy, but the total photon count diminishes due to interactions. Similar to beta particles, the reduction in intensity of a narrow photon beam as it passes through matter exhibits an exponential pattern related to the penetration depth, though with less pronounced absorption coefficients, as expressed in the Eq. 2.3 [1]:

$$I = I_0 \cdot e^{-\mu x} \tag{2.3}$$

where I_0 represents the unattenuated initial beam intensity, x is the absorber thickness, and μ is the attenuation coefficient. In contrast to betas, photons lack a definite maximum range. The ratio I/I_0 signifies the fraction of photons remaining after traversing a depth x into the absorber. The total probability of interaction combines the individual contributions of Compton scatter ($\sigma_{Compton}$) and photoelectric absorption (τ_{Photo}) cross-sections, as depicted in the Eq. 2.4 [1]:

$$\sigma_T = Z \cdot \sigma_{Compton} + \tau_{Photo} \tag{2.4}$$

To determine the total contribution of Compton scattering, the interaction cross-section is multiplied by the atomic number Z, which represents the number of electrons per atom available for scattering interactions [1].

2.4 Types of Corrections

2.4.1 Attenuation Correction

Attenuation correction is an essential process in SPECT imaging, which helps to improve the accuracy and reliability of the images by correcting for the loss of photon signal due to absorption and scattering within the body. To execute nonuniform attenuation correction, it is essential to create a patient-specific attenuation map [19]. Integrated SPECT systems, utilizing an external transmission source in different configurations, have been used with varying levels of success [19]. Advances in computer systems have supported the development of nonuniform attenuation correction meth-

ods, enabling the iterative reconstruction techniques to increasingly approximate the true tracer distribution [19].

2.4.2 Scatter Correction

The goal of estimating scatter is to obtain an accurate estimation of the actual scatter distribution without any biases. Methods based on energy distribution aim to approximate the level of scatter within a pixel designated for the photopeak energy window. This estimation is achieved by analyzing the fluctuations in counts acquired within the same pixel across one or multiple energy windows [1].

The initial scatter correction technique, the dual-energy window (DEW) method, was introduced by Jaszczak [20, 21]. This straightforward correction method based on energy distribution is applicable to both SPECT and PET images [22]. In the DEW method, two neighboring energy windows are employedâone for the photopeak and the other for scattering. The underlying assumption is that both energy windows include both scattered and unscattered coincidences [22]. In other words, the spatial distribution of counts recorded in a lower scatter window within the Compton region of the energy spectrum reflects the spatial distribution of scattered counts observed in the photopeak window [22]. Consequently, the counts recorded in the scatter window serve to estimate the scattered photons within the primary photopeak window, as depicted by part (A) in Figure 2.7 [22]. The unscattered photon counts (C_{prim}) can then be derived by subtracting the scattered photon counts (C_{sca}) from the total count (C_{tot}). This operation can be performed as follow [22]:

$$C_{prim} = C_{tot} - C_{sca} \tag{2.5}$$

The Triple Energy Window (TEW) method stands as an additional energy-centric approach employed for scatter correction in SPECT imaging. The spectral representation of the TEW method, employing a trapezoidal approximation, is illustrated in part (B) in Figure 2.7. This method involves utilizing the trapezoid-shaped

area formed by tight scatter windows (W_s) positioned on both the left and right sides of the photopeak window to estimate the contribution of Compton scattering in the photopeak energy spectrum. Here, C_{sca} denotes the counts within the windows (C_{left} and C_{right}) on either side of the photopeak window. The widths of the photopeak (main) and scatter windows, denoted as W_m and W_s, respectively, are integral to this estimation. The expression for scatter counts (C_{sca}) is shown in Eq. 2.7 [22]:

$$C_{sca} = \left(\frac{C_{left}}{W_s} + \frac{C_{right}}{W_s}\right) \cdot \frac{W_m}{2} \tag{2.6}$$

$$C_{prim} = C_{tot} - \left(\frac{C_{left}}{W_s} + \frac{C_{right}}{W_s}\right) \cdot \frac{W_m}{2} \tag{2.7}$$

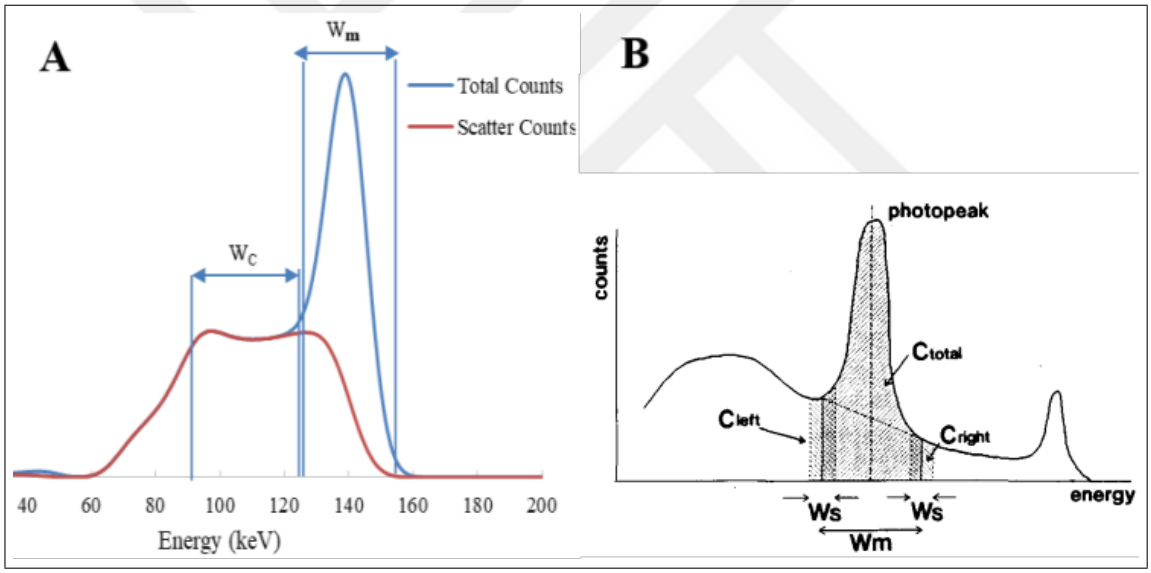


Figure 2.7 (A) Demonstration of the energy windows employed in the Dual-energy window correction method superimposed on the 99mTc energy spectrum [3]. (B) Depiction of the TEW correction method's spectral representation utilizing trapezoidal approximation [4].

Energy-distribution-based techniques that use a finite number of energy windows to create an estimate of the primary counts do not offer complete scatter compensation. This is partly a result of their use of simple geometric shapes for scatter estimation within the photopeak window. Nonetheless, the major advantages of such methods are their simplicity and speed for clinical use. Utilizing additional windows can improve performance by providing more flexibility in calculating scattering in the photopeak window.

In clinical SPECT/CT systems, numerous scatter-correction techniques predominantly utilize energy window techniques. These techniques entail estimating the scatter contribution within the photopeak window by evaluating a second energy window positioned both below and, in certain instances, above the principal photon energy. It is postulated that the scaled scatter observed in these windows adequately represents the scatter within the primary energy window. In SPECT, the utilization of multiple energy windows allows for the direct estimation of scatter through narrow energy windows positioned in immediate proximity to the photopeak. Notably, these windows may be positioned both below and above the photopeak to assess down-scatter. The ascertained scatter serves to furnish an approximation of the scatter inherent in the photopeak energy window. The triple energy window (TEW) scatter correction method presents a notable advantage in its direct measurement of scatter, encompassing scatter originating from activity beyond the field-of-viewâan aspect typically challenging to model conventionally [5].

2.5 Reconstruction Methods

2.5.1 Analytical (FBP) Reconstruction

In scintillation camera imaging, a parallel-hole collimator is commonly used, allowing the detection of photons traveling closely parallel to the hole axis. This process corresponds to a forward projection [5]. To create an image, the opposite operation, called back-projection, is performed by projecting the measured data uniformly along lines defined by a specific projection angle [5]. However, this direct back-projection results in counts being distributed uniformly along the lines of response, extending beyond the object's boundaries and causing image blurring [5]. The magnitude of blur is inversely proportional to the radial distance from the source [5]. This blurring, shown in Figure 2.9, illustrates how back-projection does not accurately reconstruct the original object and is not the inverse of the projection process [6]. To address this, a special filter called a ramp filter can be applied either as a multiplication in the Fourier frequency domain or as a convolution process in the spatial domain, helping to

mitigate the blurring effect [5].

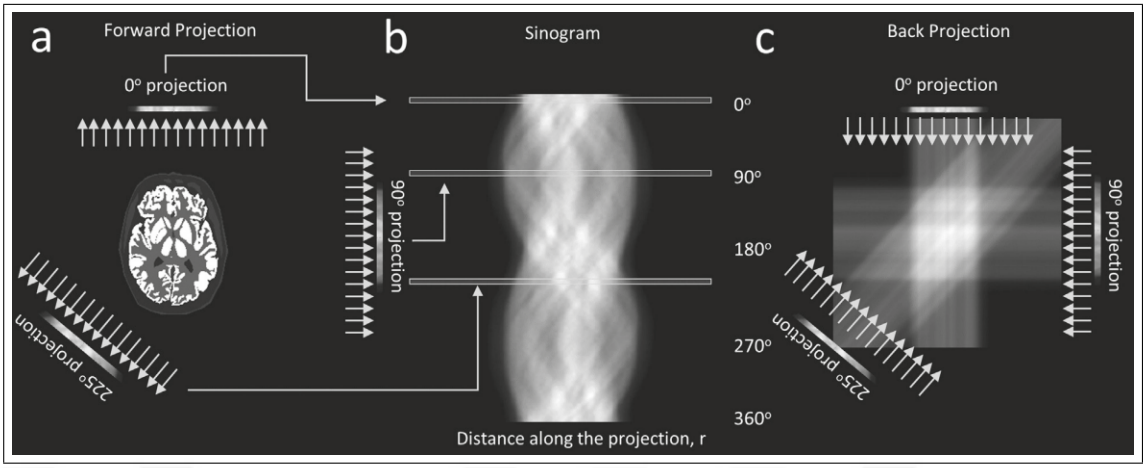


Figure 2.8 First, (a) photons are emitted in parallel directions, pass through the collimator, and form a projection image. The camera is then rotated to capture a different perspective of the same distribution. Next, (b) the acquired data is rearranged into a sinogram. Finally, (c) the data is back-projected into the object domain to produce an estimated activity distribution [5].

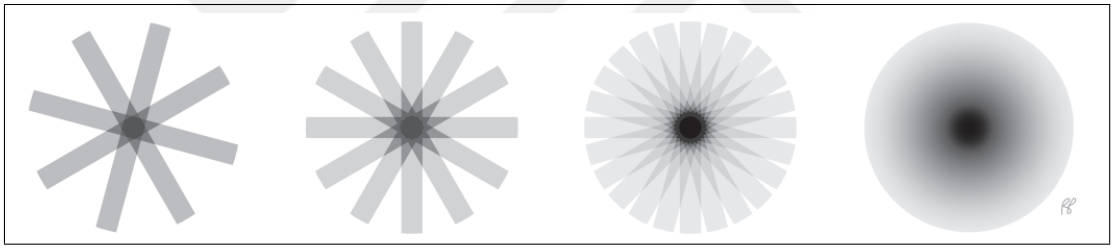


Figure 2.9 Blurring caused by FBP [6].

Opting for Fourier domain filtering is more advantageous when dealing with substantial data quantities, particularly for larger matrix sizes, due to its superior computational efficiency. Mathematically, the process of filtered back-projection can be defined as follows in Eq 2.8 [5]:

$$f(x,y) = \int_0^{\pi} F^{-1}\left[|v| \cdot F\{p(r,\theta)\}\right] d\theta \tag{2.8}$$

Where F and F^{-1} represent the Fourier transform and the inverse Fourier transform operations, respectively, and $r = x \cdot \cos(\theta) + y \cdot \sin(\theta)$. The process involves computing the Fourier transform of the projection data $p(r,\theta)$, multiplying the result by a ramp filter v, and then performing the inverse Fourier transform. Finally, the result is back-projected [5].

To obtain Eq. 2.8, we initiate the process from the definition of the 2D Fourier transform (FT) for an image f(x, y) and its corresponding inverse. The following transformations enable us to transition between the spatial and frequency domains [5].

$$\mathcal{F}^{-1} \Longleftrightarrow \mathcal{F}$$

$$f(x, y) \Longleftrightarrow F(v_x, v_y)$$

where

$$F(v_x, v_y) = \int_{-\infty}^{\infty} \int_{-\infty}^{\infty} f(x, y)\, e^{-2\pi i(xv_x + yv_y)}\, dx\, dy \tag{2.9}$$

$$f(x, y) = \int_{-\infty}^{\infty} \int_{-\infty}^{\infty} F(v_x, v_y)\, e^{2\pi i(xv_x + yv_y)}\, dv_x\, dv_y \tag{2.10}$$

where ν_x and ν_y are spatial frequency variables corresponding to spatial coordinates x and y, respectively. Setting $\nu_y = 0$ in Eq. 2.9, we get:

$$F(v_x, 0) = \int_{-\infty}^{\infty} \int_{-\infty}^{\infty} f(x, y)\, e^{-i2\pi x v_x}\, dx\, dy$$

$$= \int_{-\infty}^{\infty} \left(\int_{-\infty}^{\infty} f(x, y)\, dy \right) e^{-i2\pi x v_x}\, dx \tag{2.11}$$

Changing x to r and ν_x to ν_r, we can write:

$$= \int_{-\infty}^{\infty} p_\theta(r) \cdot e^{-i2\pi r v_r}\, dr \Big|_{\theta=0} = P_\theta(v_r)\Big|_{\theta=0} \tag{2.12}$$

where

$$p_\theta(r) = \int_{-\infty}^{\infty} f(x,y)\, ds \Big|_{x=r\cdot cos(\theta)-s\cdot sin(\theta), y=r\cdot sin(\theta)+s\cdot cos(\theta)} \tag{2.13}$$

The $p_\theta(r)$ is the forward projection (FP) of $f(x,y)$ at angle θ and $P_\theta(\nu_r)$ is its 1D Fourier Transform. The FP operator, also known as the Radon transform, is used to characterize the SPECT measurement process, excluding considerations of photon attenuation, scattering, and the distance-dependent resolution effect. A result similar to Eq. 2.12 is obtained for $\theta = \frac{\pi}{2}$ with $\nu_x = 0$ [5]. Due to rotational symmetry, the following general equality holds for any angle θ.

$$P_\theta(v_r) = F(v_x, v_y)\Big|_{v_x=v_r\cdot cos(\theta), v_y=v_r\cdot sin(\theta)} \tag{2.14}$$

In simple terms, this implies that the 1D Fourier Transform (FT) of a parallel projection at an angle θ for a 2D function is equivalent to a cross-section through the origin at the same angle θ of the 2D FT of the function. This principle is recognized as the central section theorem and is also illustrated schematically in Figure 2.10. The implication of this theorem is that, in theory, it is feasible to reconstruct an image from its Radon transform. One possible approach involves constructing the 2D FT of the image and then applying Eq. 2.10 . However, this process necessitates the interpolation of data from polar to Cartesian coordinates in the frequency domain, a task that is achievable but not straightforward [5].

2.5.2 Iterative Reconstruction (IR)

Most modern SPECT systems now offer the choice of using statistical iterative reconstruction methods to generate tomographic images, as opposed to the more traditional filtered back projection. These iterative approaches involve incorporating a computational model of both the imaging system and the patient under examination. The aim is to calculate projections in a manner analogous to how actual projections are acquired. The primary objective of this reconstruction process is to determine the

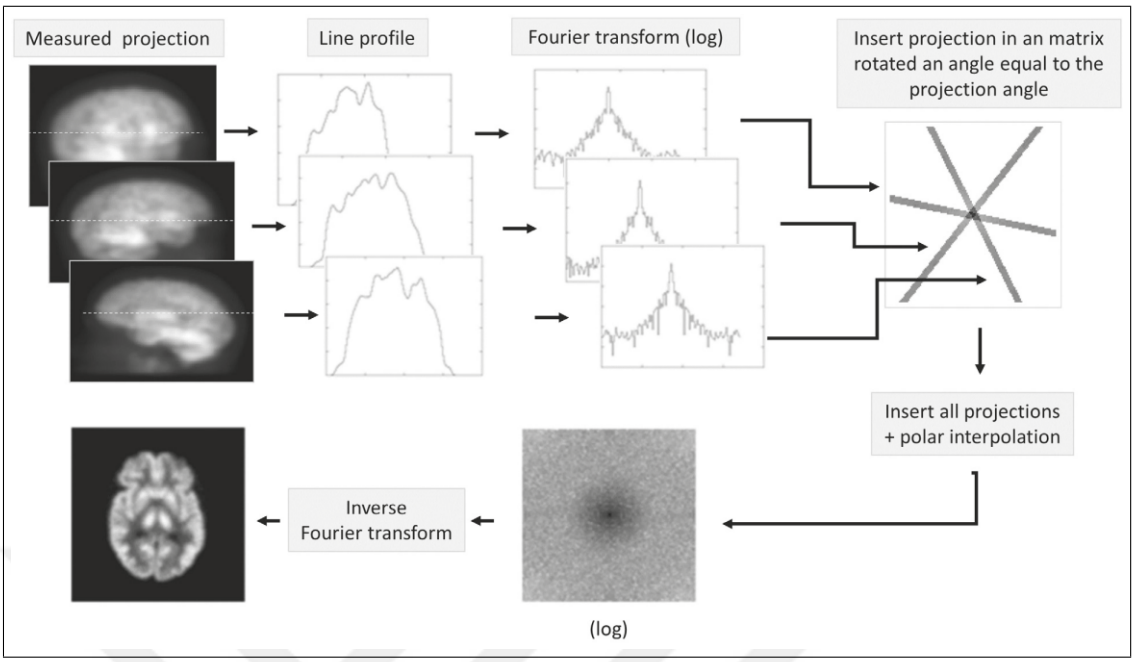


Figure 2.10 Steps of reconstruction of an object by FBP [5].

most likely estimate of the distribution of radionuclides by comparing various criteria, including the computed and measured projections. This is achieved by starting from an initial guess of the unknown source distribution, generating projection data using the model of the camera and patient, and iteratively adjusting the image estimate until the disparity between calculated and measured projections becomes sufficiently small. The fundamental assumption is that if the calculated and measured projections match, the estimate of the source distribution correctly represents the distribution of activity in the patient [5]. One of the most commonly used iterative reconstruction algorithms is Ordered-Subset Expectation-Maximization (OSEM), which will be later discussed in detail.

2.6 Ordered Subsets Expectation Maximization Algorithm

The widely employed iterative reconstruction method, known as the Maximum Likelihood Expectation Maximization (MLEM) algorithm, often requires extensive computation time when considering all projection views within each iteration for generating correction slices. To expedite the computational process, another approach,

Ordered Subsets Expectation Maximization (OSEM), is used, where a more manageable subset of matched projection views, derived from both the estimated and original datasets, is utilized in each iteration to create these correction slices. This approach involves employing a distinct subset for each iteration, with each subset comprising projection views evenly sampled across the full acquisition arc, whether it's 180 or 360 degrees [6].

For instance, in the context of a SPECT scan with 64 projections acquired over 180 degrees, let's assume the objective is to create 8 subsets for efficient computation. First, given the total of 64 projections, each covering a segment of the 180° arc, the task is to distribute these projections evenly across 8 subsets. To achieve this, a methodical approach is applied, where the process initiates with subset 1. Subset 1 encompasses projections starting with the first projection and then includes every 8th projection. Thus, subset 1 consists of projections 1, 9, 17, 25, 33, 41, 49, and 57. Similarly, in a similar manner subset 2 starts with the second projection and includes every 8th projection in the sequence, resulting in the inclusion of projections 2, 10, 18, 26, 34, 42, 50, and 58. This pattern is continued for the remaining subsets and the final subset, subset 8, is generated by starting with the eighth projection.

2.7 Monte Carlo (MC) Simulation in Medical Imaging

A critical component of Monte Carlo calculations is the random number generator. While it's possible to derive numbers from genuinely random events, such as radioactive decay, this approach is often impractical and time-consuming. True random numbers, by definition, exhibit random distributions and, as a result, are inherently unpredictable. For practical purposes, computer algorithms can generate uniformly distributed random numbers based on calculated seed values. One such algorithm is the linear congruential algorithm, which computes a sequence of random numbers (I) starting from an initial seed value (I_0). This process involves constants (a and b) and

the computer's integer word size (k) as shown in Eq. 2.9 [13].

$$I_{n+1} = (aI_n + b)\, mod\, (2^k) \tag{2.15}$$

Notably, using the same SEED value results in the same sequence of random numbers. To prevent identical outcomes in different simulations, it's essential to randomly alter the initial SEED value, ensuring variability when comparing simulations [13].

In all Monte Carlo computations, prior information about the simulated process is necessary. This information is usually represented as probability distribution functions (pdfs) for different processes. For example, when simulating photon interactions, total and partial cross-section data serve as the information needed to determine interaction type and path length. This data allows random choices to be made, such as the type of interaction or how far a photon will travel before the next interaction. Pdfs are typically defined over a range $[a, b]$, and the ideally integrable function can be normalized by integrating over its full range. To generate a stochastic variable following a specific pdf, two methods can be applied.

2.7.1 Distribution function method

A cumulative distribution function ($cpdf(x)$) is created by integrating the probability density function ($pdf(x)$) over the interval $[a, x]$, as expressed in Eq. 2.10.

$$cpdf(x) = \int_a^x pdf(x')\, dx' \tag{2.16}$$

A random sample (x) is then obtained by substituting cpdf(x) into Eq. 2.15 with a uniformly distributed random number within the range $[0, 1]$, and solving for x [13].

2.7.2 The "rejection" method

Occasionally, the distribution function method can be challenging to apply due to mathematical complexities associated with computing the cumulative probability distribution inverse (cpdf). In such situations, an alternative approach known as the rejection method can be employed, which can be summarized in three steps:

1. Begin with a probability distribution function, pdf(x), that is confined within the range $[a, b]$. Create a normalized function, pdf*(x), by dividing pdf(x) by the maximum value of pdf(x), ensuring that the maximum value of pdf* equals one.

2. Generate a random number, R_1, distributed uniformly within the range $[a, b]$ using the relationship $x = a + R_1(b - a)$.

3. Decide whether the sampled x should be accepted by generating a second random number, R_2. Calculate the value of pdf*(x) at the sampled x and check if R2 is less than pdf*(x). If this condition is met, x is accepted as a properly distributed stochastic value. Otherwise, the process is repeated, and a new x value is sampled according to the procedure outlined in step 2.

3. METHODS

3.1 The Extended Cardiac-Torso (XCAT) Phantom

In this study, the 4D XCAT digital phantom, developed by Professor Paul Segars from Duke University, was used. The XCAT phantom program provides highly detailed anatomical models for both male and female subjects at the 50th percentile in terms of height, weight, and organ volumes [23]. This versatile software supports a wide range of medical imaging and research applications [23]. Table 3.1 shows the features of the 50th percentile male phantom generated in this study. The number of frames per one cardiac cycle in gated acquisition mode is usually between 8-16 frames. Increasing the number of frames increases temporal resolution and blurring but may result in noisy images since the number of counts per frames will become lower.

3.1.1 Generation of Normal and Defective Phantoms

Using the XCAT Program, normal (healthy) and defective phantoms were created in a few steps. First the normal phantom had to be created and afterwards the lesion can be introduced in the phantom by subtracting the defect from the normal phantom in order to obtain a defective phantom. The following parameters of the digital phantom was first set in the file "general.samp.par":

1. *mode = 0 , (mode 0 = phantom, mode 1 = lesion)*
2. *hrt_period = 1 (heart cycle period, 1s)*
3. *out_frames = 8 (number of frames for one heart cycle)*
4. *gender = 0 (0 = male, 1 = female)*
5. *organ_file = vmale50.nrb (male or female phantom file)*

[h]

Table 3.1
Measurements of the 50th percentile male phantom [7].

Measurement	**Value**
Height (cm)	176.1
Weight (kg)	81
Head circumference (cm)	58.5
Waist width (cm)	30.3
Waist depth (cm)	23.4
Hip breadth (cm)	32.8

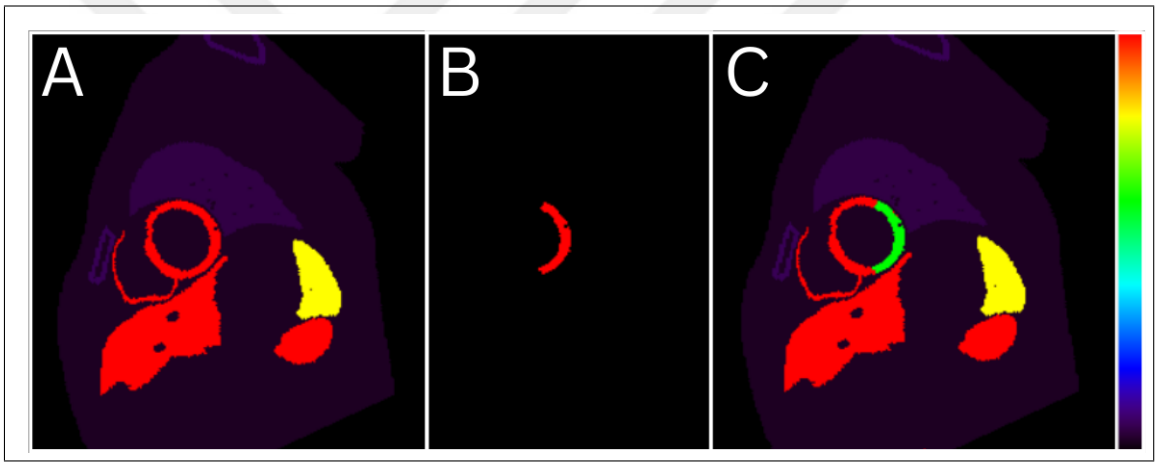


Figure 3.1 Steps of creating a defective phantom. Part A is the normal healthy phantom, part B shows the defect on its own, and part C is the result after subtraction of part B from A.

3.1.2 Activity Distribution

In the XCAT program, specifically the "general.samp.par" file, each organ is assigned an activity level, representing the biodistribution of the radiotracer to be used, in this case, Tc99m-sestamibi. Those values represent the relative uptake ratio in each organ. Table 3.2 shows the ratios for Tc99m-sestamibi radiotracer [24]. In the appendix, the variables and their uptake ratios are shown as they were set in the "general.samp.par" file.

Table 3.2
Relative Uptake Ratios in the XCAT phantom from 99mTc-MIBI

Organ(s)	**Relative Uptake Ratio**
Heart Myocardium, Liver, and Kidneys	75
Spleen	60
Lungs	4
Stomach, Ribs, Spine, and Body	2

3.2 SIMIND Monte Carlo Simulation

Two dual head SPECT cameras were simulated based on specifications of two typically used cameras, to produce images of the radiotracer distribution. Monte Carlo (MC) simulations were performed using the SIMIND (version 7.0.3) software for all frames of the phantom. SIMIND is a versatile Monte Carlo simulation code designed for modeling standard clinical Single-Photon Emission Computed Tomography (SPECT) cameras and has been rigorously validated against real SPECT cameras in many studies [25],[26],[27],[28]. Table 3.3 demonstrates the intrinsic differences between the two camera models using 99m-Technetium as a radiotracer [29],[30].

Table 3.3
Comparison of Camera 1 and Camera 2 Parameters

Component	**Parameter**	**Camera 1**	**Camera 2**
Crystal	Crystal Thickness	0.95 mm	0.95 mm
Collimator	Collimator Type	LEHR	LEHR
	Hole Shape	Hex	Hex
	Number of Holes	148,000	86,300
	Hole Length	24.05 mm	35 mm
	Hole Diameter	1.11 mm	1.5 mm
	Septal Thickness	0.16 mm	0.2 mm
	Septal Penetration	1.5%	0.3%
System	System Sensitivity (@ 100 mm)	202 cpm/μCi	160 cpm/μCi
	System Resolution (@ 100 mm)	7.5 mm	7.4 mm

3.2.1 Simulation and Acquisition

Using SIMIND, the acquisition parameters and hardware specifications and of the camera to be simulated can be set easily using the change program. For each camera, a separate ".smc" file was created which saved the parameters related to the cameras. Table 3.4 shows the general specifications that were set for both cameras.

Table 3.4
Specifications of the SPECT/CT systems used.

Parameter	**Value**
Energy Resolution (% from 140keV)	9%
Intrinsic Resolution (mm)	0.95
Number of Projections	64
Angular Range	180° (45° RAO - 45° LPO)
Image Matrix Size	128x128
Pixel Size (mm)	3.0
Source-to-detector distance	20 cm

Moreover, although the two cameras exhibited greater similarities than disparities intrinsically, there were differences in the properties of their collimators and the dimensions of their crystals. Two gamma cameras with NaI (Tl) crystals acquired projection data with a radius of rotation of 20 cm. A low-energy high-resolution (LEHR) collimator was coupled with the cameras.

3.2.2 Reconstruction and Corrections

For each frame, twelve separate processing runs were carried out, one for each selected iteration/subset pair, with and without Poisson noise included in the projections. The twelve subset-iteration parameters with which the images were reconstructed are 2-4, 2-6, 2-8, 2-16, 2-32, 4-4, 4-6, 4-8, 4-12, 8-4, 8-6, 16-2. For each camera, 192 reconstructions were performed, with a total of 384 reconstructions. In the imageâs reconstruction, the data were topographically visualized and processed in the three anatomical planes, with AMIDE (A Medical Image Data Analysis Tool) [31]. Both

attenuation and scatter corrections were applied to all images. Scatter correction was applied using the triple energy window (TEW) method in SIMIND. This approach utilizes three energy windows, including one centered around the photopeak. This methodâs performance can be optimized and adjusted based on the location and width of these windows. It is important to note that the removal of scatter photons may increase Poisson noise, which can subsequently impact lesion detectability. Table 3.5 shows the settings used for TEW scatter correction.

Table 3.5
Energy Windows and their Widths

Energy Window	**Window Width (limits)**
Upper window	2 (154-156 keV)
Lower window	2 (124-126 keV)
Photopeak window	28 (126-154 keV)

In SIMIND and CASTOR, attenuation correction can be performed by including a switch during reconstruction, this switch was included in all reconstruction runs. SIMIND produces attenuation maps in units of cm-1. For the 8 frames and the 12 OSEM parameters, scatter and attenuation corrections were performed with and without including Poisson noise in the projections.

3.3 Filtering

In image processing, selecting the appropriate filter often involves finding a balance between reducing noise, suppressing fine details, enhancing contrast, and considering the spatial frequency pattern of the image data. In a myocardial perfusion study with 99mTc sestamibi, it has been found that optimal contrast between normal and defective myocardium could be achieved using the Butterworth filter, with cutoffs ranging from 0.3 to 0.5 and orders from 3 to 9 [10]. The Butterworth filter, widely used in nuclear medicine, is defined by two key parameters (Eq. 3.1): the cut-off frequency, representing the frequency where the filter function declines towards zero (fc), and the

order (n), which determines the slope of the filter [32].

$$B(f) = \frac{1}{1 + \left(\frac{f}{f_c}\right)^{2n}} \tag{3.1}$$

This was further tested on simulated images across all frames and OSEM combinations to determine the exact order and cutoff frequency that would give the best SNR and CNR values. The optimal parameters were at an order of 3 and cut off frequency of 0.5. Interestingly, those parameters were the optimal for both cameras. Figure 3.2 shows the effect of this filter on image quality.

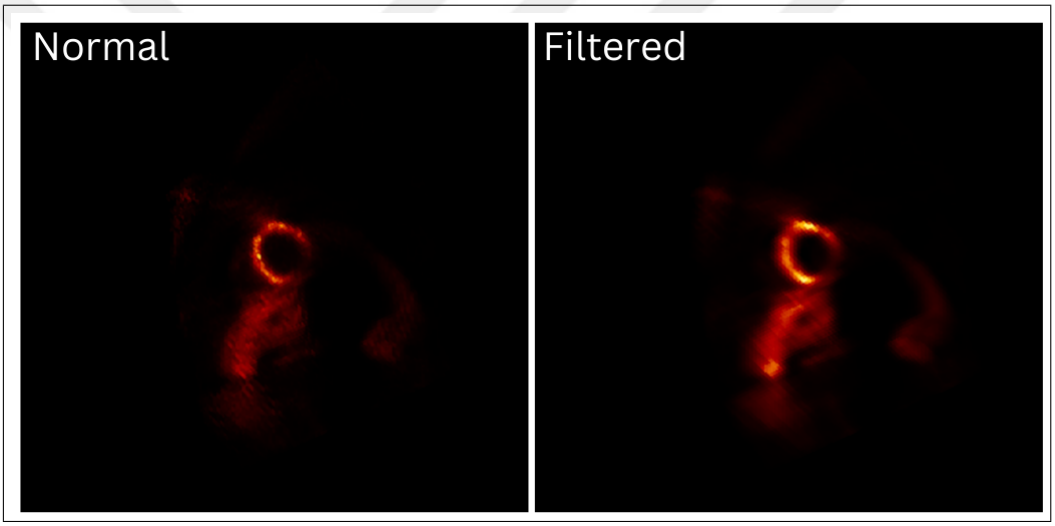


Figure 3.2 The difference in image quality after applying the butterworth filter with an order of 3 and cutoff frequency of 0.5.

3.4 Image Quality Assessment

To quantitatively assess the relationship between image quality and OSEM parameters across the 8 frames, the CNR and SNR were calculated for the reconstructed images. To achieve this, three distinct regions of interest (ROIs) were set: the healthy part of left ventricular (LV) myocardium, the anterolateral lesion, and the background. To limit variations in the results, the ROI selection depended mainly on the XCAT phantom that was developed. In other words, the mid slice of the short axis in the phantom files was selected and used to draw the ROI of the normal myocardium and

the anterolateral lesion and then those ROIs were overlayed on the reconstructed images. This was done for each frame individually. The background ROI was set on the reconstructed image directly.

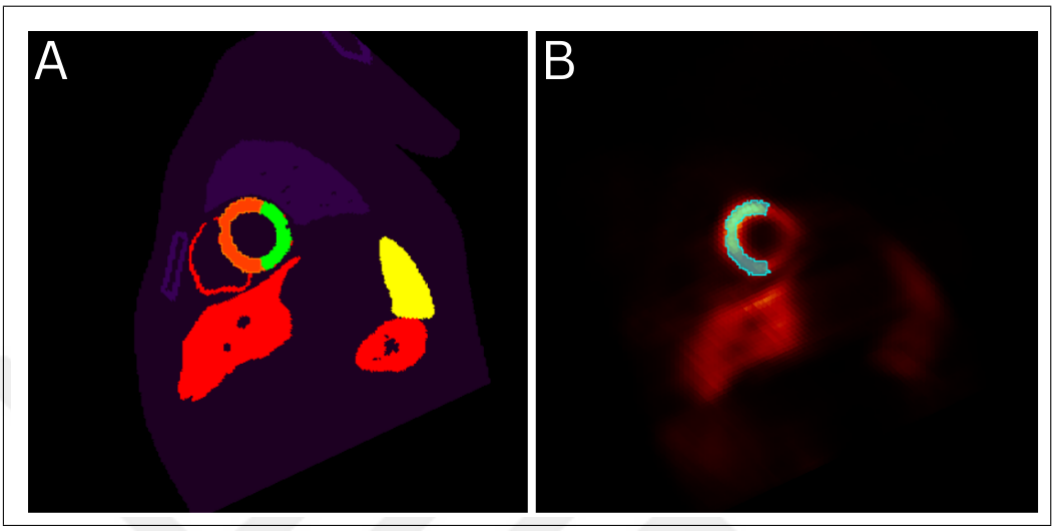


Figure 3.3 ROI selection using the Phantom file as a template. Part A shows the XCAT phantom file for frame 6 with the healthy LV ROI drawn in orange and part B shows the reconstructed image of the same frame with the same ROI overlayed.

Defect Contrast, CNR and SNR were defined as shown below [8],[33],[34].

$$DefectContrast(\%) = \frac{\mu_{MYONorm} - \mu_{MYODef}}{\mu_{MYONorm} + \mu_{MYODef}} \times 100\% \tag{3.2}$$

$$CNR = \frac{\mu_{MYONorm} - \mu_{MYODef}}{\sigma_{MYONorm}} \tag{3.3}$$

$$SNR = \frac{\mu_{MYONorm}}{\sigma_{BG}} \tag{3.4}$$

4. RESULTS

After obtaining the filtered images and selecting the ROIs, each imageâs quality metrics were assessed. For each image, twelve OSEM parameters were considered, and with each parameter, a different CNR, SNR and contrast values were obtained. In Figure 4.2, images of a single frame are shown for visual illustration of the differences between parameters across two heart planes. For each acquired image using Camera 1, the values obtained using a specific parameter were listed and compared to their corresponding values obtained using Camera 2.

The results show an increasing trend in the values of the quality metrics as the number of iterations and subsets used in the OSEM reconstruction increased. Specifically, it is evident from the results shown in Figure 4.2, that for a specific subset number, as the number of iterations increased, the image quality kept improving. Moreover, Camera 1 results in higher contrast, CNR, and SNR values compared with Camera 2.

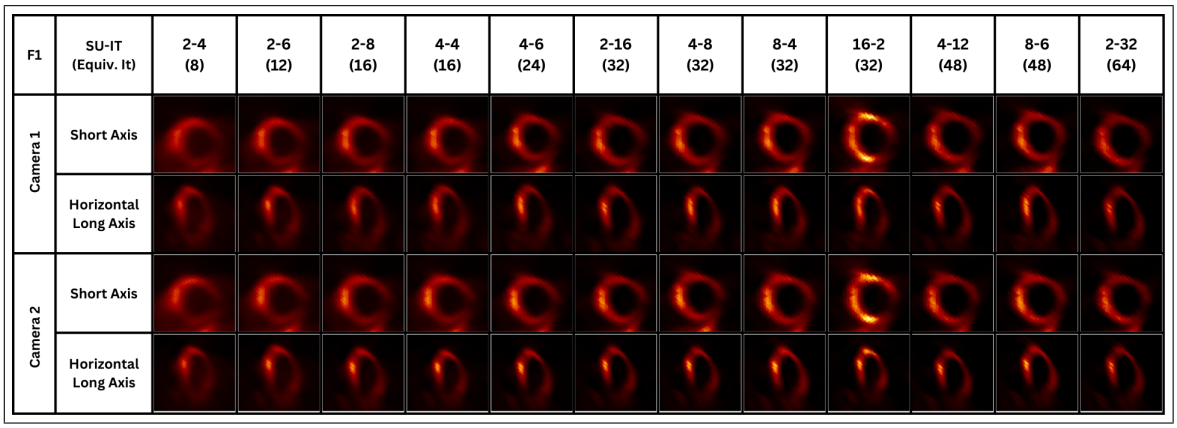


Figure 4.1 SPECT images obtained using Camera 1 and Camera 2 with different OSEM parameters

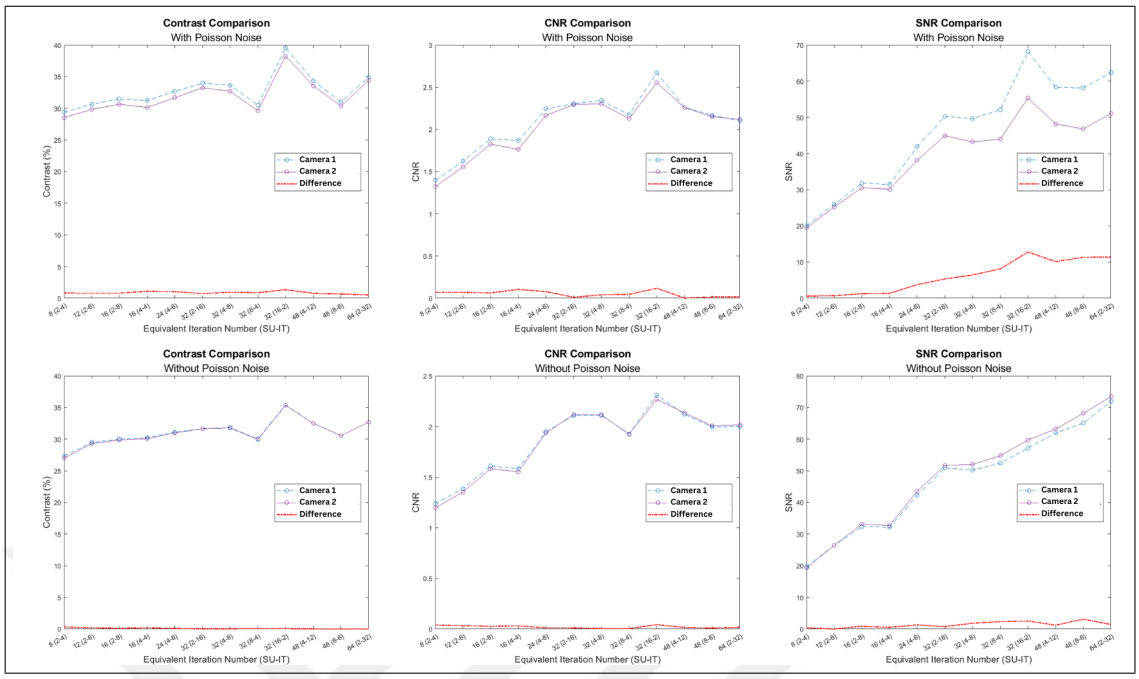


Figure 4.2 The defect contrast, CNR, and SNR values across the OSEM parameters. The first row shows those values with Poisson noise included, while the 2nd row shows the results without Poisson noise.

4.1 Statistical Analysis

Since SIMIND simulations consider the randomness of the photon interactions and therefore create different images each time, two simulations were made and reconstructed for each one frame to correctly capture the variance produced with the simulated images, resulting in a total of 16 simulations for each camera. The defect contrast, CNR, and SNR of the images were then ordered and ranked, and the Wilcoxon Signed-Rank Test was applied for statistical comparison. The test was two-tailed, and a p value of less than 0.05 was considered significant. Table 4.1 presents the average image quality metrics values obtained using both cameras across 16 images alongside the p-values for each comparison.

Table 4.1
Comparison of Defect Contrast, CNR, and SNR between Camera 1 (C1) and Camera 2 (C2).

Metric	Defect Contrast (%)				Defect CNR				SNR			
	C1	C2	Diff (%)	p-value	C1	C2	Diff (%)	p-value	C1	C2	Diff (%)	p-value
2-4	29.381	28.552	2.90%	0.00112	1.395	1.324	5.37%	0.00044	19.999	19.435	2.90%	0.01129
2-6	30.664	29.847	2.74%	0.00078	1.624	1.555	4.42%	0.00044	25.960	25.249	2.82%	0.00446
2-8	31.482	30.664	2.67%	0.00078	1.891	1.828	3.44%	0.00064	31.825	30.573	4.10%	0.00320
2-16	34.005	33.266	2.22%	0.00112	2.307	2.295	0.50%	0.67912	50.279	44.954	11.85%	0.00044
2-32	34.940	34.416	1.52%	0.01306	2.102	2.119	0.81%	0.17881	62.441	51.072	22.26%	0.00044
4-4	31.241	30.145	3.64%	0.00064	1.869	1.764	5.95%	0.00044	31.478	30.113	4.53%	0.00271
4-6	32.709	31.673	3.27%	0.00078	2.245	2.167	3.58%	0.00053	41.930	38.158	9.89%	0.00135
4-8	33.652	32.706	2.89%	0.00112	2.345	2.304	1.78%	0.00446	49.653	43.225	14.87%	0.00044
4-12	34.378	33.591	2.34%	0.00135	2.262	2.260	0.10%	0.79599	58.353	48.223	21.01%	0.00044
8-4	30.509	29.637	2.94%	0.00161	2.174	2.128	2.15%	0.00271	52.133	44.012	18.45%	0.00044
8-6	31.036	30.371	2.19%	0.00613	2.168	2.152	0.74%	0.06267	58.171	46.828	24.22%	0.00044
16-2	39.596	38.244	3.53%	0.00053	2.673	2.555	4.62%	0.00078	68.162	55.383	23.07%	0.00044

5. CONCLUSION

5.1 Findings

After the quantitative assessment by CNR of the images produced by both cameras, the present study concludes that the utilization of iterative OSEM algorithm performing 16 subsets and 2 iterations generates images with the greatest diagnostic quality for patients with average BMI and body features, followed by the combination of 2 subsets and 32 iterations, in both cameras. This shows that between the two camera models, the optimal OSEM parameter does not change. The comparison also shows a difference between the defect contrast and CNR values obtained from all twelve parameters using both cameras, as demonstrated in Table 4.1. From Figure 4.2 and the quantitative results shown in Table 3, it can be seen that the difference between CNR values were small ($\sim 5\%$). Differences in SNR values were somewhat higher, but this may be due to various factors such as different background levels caused by differences in the collimators, spatial resolution, energy resolution etc.

5.2 Clinical Significance

The use of refined parameters appears to be crucial in facilitating the reconstruction of images with enhanced diagnostic accuracy, thereby ensuring precise diagnosis and subsequent suitable and efficient treatment for the patient. OSEM is widely used clinically, as it has been shown to be superior to FBP in almost all aspects, but its optimal subsets and iteration numbers are yet to be determined and standardized for different types of SPECT imaging. This, alongside the trade-off between image quality and computational demand and processing time with each OSEM parameter, explains the significance of the research in this narrow topic and the need to establish the right reconstruction parameters for each type of SPECT imaging.

This study brings us a step closer to standardizing the OSEM parameters for cardiac SPECT and shows the consistency of those parameters accross different SPECT systems.

5.3 Comparison to literature

Unlike some studies, which rely on physician evaluations, the quantitative approach used in this study ensures more objective and reproducible results using controllable computational experiments. De Barros et al. (2015) found that four iterations and four subsets produced the best images across various BMI categories, whereas Dheer et al. (2021) identified four iterations and six subsets as optimal, especially with a Butterworth filter. In both studies, the optimal OSEM parameters were determined based on the choice of physicians and the frequency with which that parameter was picked by different observers, in comparison with the rest of the parameters examined. Although the parameters included in this study were also assessed in the literature, quantitative assessment allows for a more accurate comparison between the parameters and their effect on image quality [16],[15]. Additionally, this study differs from previous research using the more controllable Monte Carlo simulation method and using two different cameras to assess how the latter influences the optimal OSEM parameter settings and the defect detectability. Studying different cameras may also be helpful in standardizing images across clinics. In this case, we see that the optimal settings and defect detectability levels are similar while the images may have slightly differing SNRâs.

5.4 Future work and limitations

It is important to note that the study is limited for its reliance on simulation environments, which are valuable but may not fully represent the complexities of real-world clinical settings. Moreover, only a male phantom was considered in this

study, which leaves a space for uncertainty in the results when the patient is a female. Moreover, the computational power and time needed for optimizing OSEM, particularly concerning reconstruction with different pairs of subsets and iterations, should be noted. The study primarily explores the effects of different subsets and iterations within a specific parameter range, possibly leaving out various clinical scenarios. Therefore, clinical validation may be required to determine the practical applicability of the study's findings. Future research should focus on validating the findings in clinical settings with a diverse patient population, including both male and female subjects. Additionally, exploring the optimization of OSEM parameters across different camera models and incorporating other patient-specific factors, such as age and comorbidities, could provide a more comprehensive understanding of the algorithm's performance.

APPENDIX A. SIMIND SIMULATIONS

A.1 Simulating the 1st Frame using Camera 1

```
 Phantom(S): h2o       Crystal...: nai       InputFile.: SymbiaT2
 Phantom(B): bone      BackScatt.: pmt       OutputFile: smd_antlathla_f1
 Collimator: pb_sb2    SourceRout: smap      SourceFile: antlathla_act_1
 Cover.....: al        ScoreRout.: scattwin  DensityMap: normphan_atn_1
-------------------------------------------------------------------
 PhotonEnergy.......: 140          tc99m    PhotonsPerProj....: 66047685
 EnergyResolution...: 9            sy-lehr  Activity..........: 1
 MaxScatterOrder....: 3            SPECT    DetectorLenght....: 29.55
 DetectorWidth......: 22.25        BScatt   DetectorHeight....: 0.953
 UpperEneWindowTresh: 154          Random   Distance to det...: 20
 LowerEneWindowTresh: 126          Cover    ShiftSource X.....: 0
 PixelSize  I.......: 0.3          Phantom  ShiftSource Y.....: 0
 PixelSize  J.......: 0.3          Resolut  ShiftSource Z.....: 0
 HalfLength S.......: 19.2         Header   HalfLength P......: 19.2
 HalfWidth  S.......: 0            SaveMap  HalfWidth  P......: 0
 HalfHeight S.......: 0                     HalfHeight P......: 0
 SourceType.........: XcatBinMap            PhantomType.......: XcatBinMap
-------------------------------------------------------------------
 GENERAL DATA
 keV/channel........: 0.5                   CutoffEnergy......: 0
 Photons/Bq.........: 0.89821               StartingAngle.....: -45
 CameraOffset X.....: 0                     CoverThickness....: 0.1
 CameraOffset Y.....: 0                     BackscatterThickn.: 6.6
 MatrixSize I.......: 128                   IntrinsicResolut..: 0.34
 MatrixSize J.......: 128                   AcceptanceAngle...: 3.05059
 Emission type......: 2                     Initial Weight....: 0.0136
 NN ScalingFactor...: 1                     Energy Channels...: 512
-------------------------------------------------------------------
 SPECT DATA
 RotationMode.......: 180                   Nr of Projections.: 64
 RotationAngle......: 2.8125                Projection.[start]: 1
 Orbital fraction...: 1                     Projection...[end]: 64
```

```
-----------------------------------------------------------------
 COLLIMATOR DATA FOR ROUTINE: Analytical
 CollimatorCode.....: sy-lehr              CollimatorType....: Parallel
 HoleSize X.........: 0.111                Distance X........: 0.016
 HoleSize Y.........: 0.12817              Distance Y........: 0.07794
 CenterShift X......: 0.10999              X-Ray flag........: F
 CenterShift Y......: 0.0635               CollimThickness...: 2.405
 HoleShape..........: Hexagonal            Space Coll2Det....: 0
 CollDepValue [57]..: 0                    CollDepValue [58].: 0
 CollDepValue [59]..: 0                    CollDepValue [60].: 0
-----------------------------------------------------------------
 IMAGE-BASED PHANTOM DATA
 RotationCentre.....: 129,129              Bone definition...: 1170
 CT-Pixel size......: 0.15                 Slice thickness...: 0.15
 StartImage.........: 1                    No of CT-Images...: 256
 MatrixSize I.......: 256                  CTmapOrientation..: 0
 MatrixSize J.......: 256                  StepSize..........: 0.1
 CenterPoint I......: 129                  ShiftPhantom X....: 0
 CenterPoint J......: 129                  ShiftPhantom Y....: 0
 CenterPoint K......: 129                  ShiftPhantom Z....: 0
-----------------------------------------------------------------
  Photon energy       Abundance
     20.669 keV       0.1120E-01
     21.023 keV       0.1770E-02
     89.600 keV       0.1040E-04
    140.511 keV       0.8850
    142.683 keV       0.2300E-03
    232.700 keV       0.8400E-07
    322.400 keV       0.9600E-06
-----------------------------------------------------------------
  Scattwin results: Window file: SymbiaT2.win

  Win  WinAdded  Range(keV)   ScaleFactor
   1       0    126.0 - 154.0    1.00
   2       0    154.0 - 156.0    7.00
   3       0    124.0 - 126.0    7.00

  Win    Total    Scatter   Primary  S/P-Ratio S/T Ratio  Cps/MBq
```

```
  1   0.164E+04 0.523E+03 0.112E+04 0.468E+00 0.319E+00 0.256E+02
  2   0.482E+01 0.305E+00 0.451E+01 0.676E-01 0.633E-01 0.752E-01
  3   0.767E+02 0.678E+02 0.888E+01 0.764E+01 0.884E+00 0.120E+01

 Win  Geo(Air)  Pen(Air)  Sca(Air)  Geo(Tot)  Pen(Tot)  Sca(Tot)
  1   100.00%     0.00%     0.00%   100.00%     0.00%     0.00%
  2   100.00%     0.00%     0.00%   100.00%     0.00%     0.00%
  3   100.00%     0.00%     0.00%   100.00%     0.00%     0.00%

 Win   SC 1  SC 2  SC 3
  1   83.0% 15.1%  1.9%
  2   95.9%  3.9%  0.2%
  3   68.4% 26.5%  5.1%
-----------------------------------------------------------------------
 INTERACTIONS IN THE CRYSTAL
 MaxValue spectrum..: 33.00
 MaxValue projection: 0.8987E-02
 CountRate spectrum.: 45.19
 CountRate E-Window.: 25.61
-----------------------------------------------------------------------
 PHOTONS AFTER COLLIMATOR AND WITHIN ENER-WIN
 Geometric..........:   0.00 %         100.00 %
 Penetration........:   0.00 %           0.00 %
 Scatter in collim..:   0.00 %           0.00 %
 X-rays in collim...:   0.00 %           0.00 %
-----------------------------------------------------------------------
 SCATTER IN ENERGY WINDOW
 Scatter/Primary....: 0.46841
 Scatter/Total......: 0.31899
 Scatter order 1....: 82.96 %
 Scatter order 2....: 15.12 %
 Scatter order 3....: 1.92 %
-----------------------------------------------------------------------
 CALCULATED DETECTOR PARAMETERS
 Efficiency E-Window: 0.4359
 Efficiency spectrum: 0.7692
 Sensitivity Cps/MBq: 25.6055
 Sensitivity Cpm/uCi: 56.8443
```

```
------------------------------------------------------------------
 Simulation started.: 2024:03:09 03:09:12
 Simulation stopped.: 2024:03:09 10:03:42
 Elapsed time.......: 6 h, 54 m and 30 s
 DetectorHits.......: 166867934
 DetectorHits/CPUsec: 7312
------------------------------------------------------------------
```

A.1.1 Reconstruction Run for 16-2 Parameter

```
PS C:\Users\User\OneDrive\Desktop\Thesis\SIMIND>
smc2castor smd_antlathla_f1_tot_w1.h00
csmd_antlathla_f1_ACSCNO_su16
smd_antlathla_f1_tew_w3.h00/run/AC/NO/MB:370/AT:20/SU:16/IT:2

C:\Users\ghass\OneDrive\Desktop\Thesis\SIMIND>
castor-recon -df smd_antlathla_f1_tot_w1.cdh -fout csmd_antlathla_f1_ACSCNO_su16
-atn smd_antlathla_f1.hct -it 2:16 -oit 2:2 -dim 128,128,128
-vox 3.00,3.00,3.00 -conf C:\Users\ghass\OneDrive\Desktop\Thesis\castor\config
-vb 1 -opti MLEM -proj classicSiddon -flip-out Y
sOutputManager::InitOutputDirectory() -> Output path is
'csmd_antlathla_f1_ACSCNO_su16'
oProjectorManager::Initialize() -> Initialize projectors and
projection lines
oOptimizerManager::Initialize() -> Initialize optimizer and penalty
iOptimizerMLEM::Initialize() -> Use the MLEM optimizer
oIterativeAlgorithm::IterateCPU() -> Start algorithm for 2 iterations
oIterativeAlgorithm::IterateCPU() -> Start iteration 1/2 subset 1/16
oIterativeAlgorithm::IterateCPU() -> Start iteration 1/2 subset 2/16
oIterativeAlgorithm::IterateCPU() -> Start iteration 1/2 subset 3/16
oIterativeAlgorithm::IterateCPU() -> Start iteration 1/2 subset 4/16
oIterativeAlgorithm::IterateCPU() -> Start iteration 1/2 subset 5/16
oIterativeAlgorithm::IterateCPU() -> Start iteration 1/2 subset 6/16
oIterativeAlgorithm::IterateCPU() -> Start iteration 1/2 subset 7/16
oIterativeAlgorithm::IterateCPU() -> Start iteration 1/2 subset 8/16
oIterativeAlgorithm::IterateCPU() -> Start iteration 1/2 subset 9/16
oIterativeAlgorithm::IterateCPU() -> Start iteration 1/2 subset 10/16
```

```
oIterativeAlgorithm::IterateCPU() -> Start iteration 1/2 subset 11/16
oIterativeAlgorithm::IterateCPU() -> Start iteration 1/2 subset 12/16
oIterativeAlgorithm::IterateCPU() -> Start iteration 1/2 subset 13/16
oIterativeAlgorithm::IterateCPU() -> Start iteration 1/2 subset 14/16
oIterativeAlgorithm::IterateCPU() -> Start iteration 1/2 subset 15/16
oIterativeAlgorithm::IterateCPU() -> Start iteration 1/2 subset 16/16
oIterativeAlgorithm::IterateCPU() -> Start iteration 2/2 subset 1/16
oIterativeAlgorithm::IterateCPU() -> Start iteration 2/2 subset 2/16
oIterativeAlgorithm::IterateCPU() -> Start iteration 2/2 subset 3/16
oIterativeAlgorithm::IterateCPU() -> Start iteration 2/2 subset 4/16
oIterativeAlgorithm::IterateCPU() -> Start iteration 2/2 subset 5/16
oIterativeAlgorithm::IterateCPU() -> Start iteration 2/2 subset 6/16
oIterativeAlgorithm::IterateCPU() -> Start iteration 2/2 subset 7/16
oIterativeAlgorithm::IterateCPU() -> Start iteration 2/2 subset 8/16
oIterativeAlgorithm::IterateCPU() -> Start iteration 2/2 subset 9/16
oIterativeAlgorithm::IterateCPU() -> Start iteration 2/2 subset 10/16
oIterativeAlgorithm::IterateCPU() -> Start iteration 2/2 subset 11/16
oIterativeAlgorithm::IterateCPU() -> Start iteration 2/2 subset 12/16
oIterativeAlgorithm::IterateCPU() -> Start iteration 2/2 subset 13/16
oIterativeAlgorithm::IterateCPU() -> Start iteration 2/2 subset 14/16
oIterativeAlgorithm::IterateCPU() -> Start iteration 2/2 subset 15/16
oIterativeAlgorithm::IterateCPU() -> Start iteration 2/2 subset 16/16
oIterativeAlgorithm::StepAfterSubsetLoop() -> Save image at iteration 2
oIterativeAlgorithm::IterateCPU() -> Total time spent | User: 92 sec
| CPU: 9.205300e+001 sec
```

A.2 Simulating the 1st Frame using Camera 2

```
 Phantom(S): h2o       Crystal...: nai       InputFile.: Hawkeye4
 Phantom(B): bone      BackScatt.: pmt       OutputFile: smd_ge_antlathla_f
 Collimator: pb_sb2    SourceRout: smap      SourceFile: antlathla_act_1
 Cover.....: al        ScoreRout.: scattwin  DensityMap: normphan_atn_1
-----------------------------------------------------------------
 PhotonEnergy.......: 140          tc99m    PhotonsPerProj....: 66047685
 EnergyResolution...: 9            gi-lehr  Activity..........: 1
 MaxScatterOrder....: 3            SPECT    DetectorLenght....: 27
```

```
 DetectorWidth......: 20          BScatt   DetectorHeight....: 0.953
 UpperEneWindowTresh: 154         Random   Distance to det...: 20
 LowerEneWindowTresh: 126         Cover    ShiftSource X.....: 0
 PixelSize  I.......: 0.3         Phantom  ShiftSource Y.....: 0
 PixelSize  J.......: 0.3         Resolut  ShiftSource Z.....: 0
 HalfLength S.......: 19.2        Header   HalfLength P......: 19.2
 HalfWidth  S.......: 0           SaveMap  HalfWidth  P......: 0
 HalfHeight S.......: 0                    HalfHeight P......: 0
 SourceType.........: XcatBinMap           PhantomType.......: XcatBinMap
-----------------------------------------------------------------------
 GENERAL DATA
 keV/channel........: 0.5                  CutoffEnergy......: 0
 Photons/Bq.........: 0.89821              StartingAngle.....: -45
 CameraOffset X.....: 0                    CoverThickness....: 0.1
 CameraOffset Y.....: 0                    BackscatterThickn.: 6.6
 MatrixSize I.......: 128                  IntrinsicResolut..: 0.34
 MatrixSize J.......: 128                  AcceptanceAngle...: 2.83317
 Emission type......: 2                    Initial Weight....: 0.0136
 NN ScalingFactor...: 1                    Energy Channels...: 512
-----------------------------------------------------------------------
 SPECT DATA
 RotationMode.......: 180                  Nr of Projections.: 64
 RotationAngle......: 2.8125               Projection.[start]: 1
 Orbital fraction...: 1                    Projection...[end]: 64
-----------------------------------------------------------------------
 COLLIMATOR DATA FOR ROUTINE: Analytical
 CollimatorCode.....: gi-lehr              CollimatorType....: Parallel
 HoleSize X.........: 0.15                 Distance X........: 0.02
 HoleSize Y.........: 0.17321              Distance Y........: 0.10392
 CenterShift X......: 0.085                X-Ray flag........: F
 CenterShift Y......: 0.14722              CollimThickness...: 3.5
 HoleShape..........: Hexagonal            Space Coll2Det....: 0
 CollDepValue [57]..: 0                    CollDepValue [58].: 0
 CollDepValue [59]..: 0                    CollDepValue [60].: 0
-----------------------------------------------------------------------
 IMAGE-BASED PHANTOM DATA
 RotationCentre.....: 129,129              Bone definition...: 1170
 CT-Pixel size......: 0.15                 Slice thickness...: 0.15
```

```
 StartImage.........: 1                    No of CT-Images...: 256
 MatrixSize I.......: 256                  CTmapOrientation..: 0
 MatrixSize J.......: 256                  StepSize..........: 0.1
 CenterPoint I......: 129                  ShiftPhantom X....: 0
 CenterPoint J......: 129                  ShiftPhantom Y....: 0
 CenterPoint K......: 129                  ShiftPhantom Z....: 0
-----------------------------------------------------------------------
  Photon energy       Abundance
     20.669 keV       0.1120E-01
     21.023 keV       0.1770E-02
     89.600 keV       0.1040E-04
    140.511 keV       0.8850
    142.683 keV       0.2300E-03
    232.700 keV       0.8400E-07
    322.400 keV       0.9600E-06
-----------------------------------------------------------------------
  Scattwin results: Window file: Hawkeye4.win

  Win  WinAdded  Range(keV)   ScaleFactor
   1       0    126.0 - 154.0    1.00
   2       0    154.0 - 156.0    7.00
   3       0    124.0 - 126.0    7.00

  Win    Total    Scatter   Primary  S/P-Ratio S/T Ratio  Cps/MBq
   1   0.144E+04 0.459E+03 0.981E+03 0.468E+00 0.319E+00 0.225E+02
   2   0.423E+01 0.269E+00 0.396E+01 0.678E-01 0.635E-01 0.661E-01
   3   0.674E+02 0.596E+02 0.780E+01 0.764E+01 0.884E+00 0.105E+01

  Win  Geo(Air)  Pen(Air)  Sca(Air)  Geo(Tot)  Pen(Tot)  Sca(Tot)
   1   100.00%     0.00%     0.00%   100.00%     0.00%     0.00%
   2   100.00%     0.00%     0.00%   100.00%     0.00%     0.00%
   3   100.00%     0.00%     0.00%   100.00%     0.00%     0.00%

  Win   SC 1  SC 2  SC 3
   1   83.0% 15.1%  1.9%
   2   96.0%  3.9%  0.2%
   3   68.4% 26.5%  5.1%
-----------------------------------------------------------------------
```

```
 INTERACTIONS IN THE CRYSTAL
 MaxValue spectrum..: 28.80
 MaxValue projection: 0.8025E-02
 CountRate spectrum.: 39.31
 CountRate E-Window.: 22.50
-----------------------------------------------------------------
 PHOTONS AFTER COLLIMATOR AND WITHIN ENER-WIN
 Geometric.....:   0.00 %         100.00 %
 Penetration.....:   0.00 %           0.00 %
 Scatter in collim..:   0.00 %           0.00 %
 X-rays in collim...:   0.00 %           0.00 %
-----------------------------------------------------------------
 SCATTER IN ENERGY WINDOW
 Scatter/Primary....: 0.46839
 Scatter/Total......: 0.31898
 Scatter order 1....: 82.96 %
 Scatter order 2....: 15.12 %
 Scatter order 3....: 1.92 %
-----------------------------------------------------------------
 CALCULATED DETECTOR PARAMETERS
 Efficiency E-Window: 0.436
 Efficiency spectrum: 0.7616
 Sensitivity Cps/MBq: 22.5034
 Sensitivity Cpm/uCi: 49.9575
-----------------------------------------------------------------
 Simulation started.: 2024:03:16 12:37:24
 Simulation stopped.: 2024:03:16 19:59:13
 Elapsed time.......: 7 h, 21 m and 49 s
 DetectorHits.......: 166847596
 DetectorHits/CPUsec: 10628
-----------------------------------------------------------------
```

A.2.1 Reconstruction Run for 16-2 Parameter

```
PS C:\Users\User\OneDrive\Desktop\Thesis\SIMIND>
smc2castor smd_ge_antlathla_f1_tot_w1.h00 csmd_ge_antlathla_f1_ACSCNO_su16
smd_ge_antlathla_f1_tew_w3.h00/run/AC/NO/MB:370/AT:20/SU:16/IT:2
```

```
C:\Users\User\OneDrive\Desktop\Thesis\SIMIND>
castor-recon -df smd_ge_antlathla_f1_tot_w1.cdh -fout
csmd_ge_antlathla_f1_ACSCNO_su16
-atn smd_ge_antlathla_f1.hct -it 2:16 -oit 2:2 -dim 128,128,128
-vox 3.00,3.00,3.00 -conf
C:\Users\User\OneDrive\Desktop\Thesis\castor\config
-vb 1 -opti MLEM -proj classicSiddon -flip-out Y
sOutputManager::InitOutputDirectory() -> Output path is
'csmd_ge_antlathla_f1_ACSCNO_su16'
oProjectorManager::Initialize() -> Initialize projectors and projection lines
oOptimizerManager::Initialize() -> Initialize optimizer and penalty
iOptimizerMLEM::Initialize() -> Use the MLEM optimizer
oIterativeAlgorithm::IterateCPU() -> Start algorithm for 2 iterations
oIterativeAlgorithm::IterateCPU() -> Start iteration 1/2 subset 1/16
oIterativeAlgorithm::IterateCPU() -> Start iteration 1/2 subset 2/16
oIterativeAlgorithm::IterateCPU() -> Start iteration 1/2 subset 3/16
oIterativeAlgorithm::IterateCPU() -> Start iteration 1/2 subset 4/16
oIterativeAlgorithm::IterateCPU() -> Start iteration 1/2 subset 5/16
oIterativeAlgorithm::IterateCPU() -> Start iteration 1/2 subset 6/16
oIterativeAlgorithm::IterateCPU() -> Start iteration 1/2 subset 7/16
oIterativeAlgorithm::IterateCPU() -> Start iteration 1/2 subset 8/16
oIterativeAlgorithm::IterateCPU() -> Start iteration 1/2 subset 9/16
oIterativeAlgorithm::IterateCPU() -> Start iteration 1/2 subset 10/16
oIterativeAlgorithm::IterateCPU() -> Start iteration 1/2 subset 11/16
oIterativeAlgorithm::IterateCPU() -> Start iteration 1/2 subset 12/16
oIterativeAlgorithm::IterateCPU() -> Start iteration 1/2 subset 13/16
oIterativeAlgorithm::IterateCPU() -> Start iteration 1/2 subset 14/16
oIterativeAlgorithm::IterateCPU() -> Start iteration 1/2 subset 15/16
oIterativeAlgorithm::IterateCPU() -> Start iteration 1/2 subset 16/16
oIterativeAlgorithm::IterateCPU() -> Start iteration 2/2 subset 1/16
oIterativeAlgorithm::IterateCPU() -> Start iteration 2/2 subset 2/16
oIterativeAlgorithm::IterateCPU() -> Start iteration 2/2 subset 3/16
oIterativeAlgorithm::IterateCPU() -> Start iteration 2/2 subset 4/16
oIterativeAlgorithm::IterateCPU() -> Start iteration 2/2 subset 5/16
oIterativeAlgorithm::IterateCPU() -> Start iteration 2/2 subset 6/16
oIterativeAlgorithm::IterateCPU() -> Start iteration 2/2 subset 7/16
oIterativeAlgorithm::IterateCPU() -> Start iteration 2/2 subset 8/16
```

```
oIterativeAlgorithm::IterateCPU() -> Start iteration 2/2 subset 9/16
oIterativeAlgorithm::IterateCPU() -> Start iteration 2/2 subset 10/16
oIterativeAlgorithm::IterateCPU() -> Start iteration 2/2 subset 11/16
oIterativeAlgorithm::IterateCPU() -> Start iteration 2/2 subset 12/16
oIterativeAlgorithm::IterateCPU() -> Start iteration 2/2 subset 13/16
oIterativeAlgorithm::IterateCPU() -> Start iteration 2/2 subset 14/16
oIterativeAlgorithm::IterateCPU() -> Start iteration 2/2 subset 15/16
oIterativeAlgorithm::IterateCPU() -> Start iteration 2/2 subset 16/16
oIterativeAlgorithm::StepAfterSubsetLoop() -> Save image at iteration 2
oIterativeAlgorithm::IterateCPU() -> Total time spent | User: 92 sec
| CPU: 9.205300e+001 sec
```

APPENDIX B. XCAT PHANTOM PROGRAM

```
myoLV_act = 75 # hrt_myoLV_act - activity in left ventricle myocardium
myoRV_act = 75 # hrt_myoRV_act - activity in right ventricle myocardium
myoLA_act = 75 # hrt_myoLA_act - activity in left atrium myocardium
myoRA_act = 75 # hrt_myoRA_act - activity in right atrium myocardium
bldplLV_act = 2 # hrt_bldplLV_act - activity in LV chamber (blood pool)
bldplRV_act = 2 # hrt_bldplRV_act - activity in RV chamber (blood pool)
bldplLA_act = 2 # hrt_bldplLA_act - activity in LA chamber (blood pool)
bldplRA_act = 2 # hrt_bldplRA_act - activity in RA chamber (blood pool)

coronary_art_activity = 2 # activity in the coronary arteries
coronary_vein_activity = 2 # activity in the coronary veins

valve_thickness = 0.1 # thickness of the AV valves (cm);

body_activity = 2 # body_activity (background activity);
skin_activity = 2 # skin_activity (used if skin_thickness is > 0)
rbreast_activity = 2 # right breast activity;
lbreast_activity = 2 # left breast activity;
muscle_activity = 2 # muscle activity;
brain_activity = 2 # brain activity;
sinus_activity = 2 # sinus activity;
liver_activity = 75.0 # liver_activity;
gall_bladder_activity = 2 # gall_bladder_activity;
r_lung_activity = 4 # right_lung_activity;
l_lung_activity = 4             # left_lung_activity;
esophagus_activity = 2 # esophagus_activity;
esophagus_cont_activity = 2 # esophagus_contents_activity
laryngopharynx_activity = 2 # laryngopharynx_activity
larynx_activity = 2 # larynx_activity
st_wall_activity = 2 # st_wall_activity;  (stomach wall)
st_cnts_activity = 2 # st_cnts_activity;   (stomach contents)
pancreas_activity = 2 # pancreas_activity;
r_kidney_cortex_activity = 75 # right_kidney_cortex_activity;
r_kidney_medulla_activity = 75 # right_kidney_medulla_activity;
```

```
l_kidney_cortex_activity = 75 # left_kidney_cortex_activity;
l_kidney_medulla_activity = 75 # left_kidney_medulla_activity;
adrenal_activity = 2 # adrenal_activity;
r_renal_pelvis_activity = 2 # right_renal_pelvis_activity;
l_renal_pelvis_activity = 2     # left_renal_pelvis_activity;
spleen_activity = 60 # spleen_activity;
rib_activity = 2 # rib_activity;
cortical_bone_activity = 5 # cortical_bone_activity;
spine_activity = 2 # spine_activity;
spinal_cord_activity = 2 # spinal_cord_activity;
bone_marrow_activity = 2 # bone_marrow_activity;
art_activity = 2 # artery_activity;
vein_activity = 2 # vein_activity;
bladder_activity = 2 # bladder_activity;
prostate_activity = 2 # prostate_activity;
asc_li_activity = 2 # ascending_large_intest_activity;
trans_li_activity = 2 # transcending_large_intest_activity;
desc_li_activity = 2 # desc_large_intest_activity;
sm_intest_activity = 2 # small_intest_activity;
rectum_activity = 2 # rectum_activity;
sem_activity = 2 # sem_vess_activity;
vas_def_activity = 2 # vas_def_activity;
test_activity = 2 # testicular_activity;
penis_activity = 2 # penis_activity
epididymus_activity = 2 # epididymus_activity;
ejac_duct_activity = 2 # ejaculatory_duct_activity;
pericardium_activity = 2      # pericardium activity;
cartilage_activity = 2 # cartilage activity;
intest_air_activity = 2.0 # activity of intestine contents (air);
ureter_activity = 2.0 # ureter activity;
urethra_activity = 2.0 # urethra activity;
lymph_activity = 2.0 # lymph normal activity;
lymph_abnormal_activity = 2.0 # lymph abnormal activity;
trach_bronch_activity = 4.0 # trachea_bronchi_activity;
airway_activity = 2.0 # airway tree activity
uterus_activity = 2 # uterus_activity;
vagina_activity = 2 # vagina_activity;
right_ovary_activity = 2 # right_ovary_activity;
```

```
left_ovary_activity = 2 # left_ovary_activity;
fallopian_tubes_activity = 2 # fallopian tubes_activity;
parathyroid_activity = 2 # parathyroid_activity;
thyroid_activity = 2 # thyroid_activity;
thymus_activity = 2 # thymus_activity;
salivary_activity = 2 # salivary_activity;
pituitary_activity = 2 # pituitary_activity;
eye_activity = 2 # eye_activity;
lens_activity = 2 # eye_lens_activity;
lesn_activity = 30 # activity for heart lesion, plaque, or spherical lesion
Corpus_Callosum_act = 8 # activity of Corpus_Callosum
Caudate_act = 16 # activity of Caudate
Internal_capsule_act = 8 # activity of Internal_capsule
Putamen_act = 16 # activity of Putamen
Globus_pallidus_act = 16 # activity of Globus_pallidus
Thalamus_act = 8 # activity of Thalamus
Fornix_act = 8 # activity of Fornix
Anterior_commissure_act = 8 # activity of Anterior_commissure
Amygdala_act = 16 # activity of Amygdala
Hippocampus_act = 16 # activity of Hippocampus
Lateral_ventricle_act = 8 # activity of Lateral_ventricle
Third_ventricle_act = 8 # activity of Third_ventricle
Fourth_ventricle_act = 8 # activity of Fourth_ventricle
Cerebral_aqueduct_act = 8 # activity of Cerebral_aqueduct
Mamillary_bodies_act = 8 # activity of Mamillary_bodies
Cerebral_peduncles_act = 8 # activity of Cerebral_peduncles
Superior_colliculus_act = 8 # activity of Superior_colliculus
Inferior_colliculus_act = 8 # activity of Inferior_colliculus
Pineal_gland_act = 8 # activity of Pineal_gland
Periacquaductal_grey_outer_act = 16 # activity of Periacquaductal_grey_outer
Periacquaductal_grey_act = 16 # activity of Periacquaductal_grey_inner
Pons_act = 8 # activity of Pons
Superior_cerebellar_peduncle_act = 8 # activity of Superior_cerebellar_peduncle
Middle_cerebellar_peduncle_act = 8 # activity of Middle_cerebellar_peduncle
Substantia_nigra_act = 16 # activity of Substantia_nigra
Medulla_act = 8 # activity of Medulla
Medullary_pyramids_act = 8 # activity of Medullary_pyramids
Inferior_olive_act = 8 # activity of Inferior_olive
```

```
Tegmentum_of_midbrain_act = 8 # activity of Tegmentum_of_midbrain
Midbrain_act = 8 # activity of Midbrain
cerebellum_act = 8 # activity of cerebellum
white_matter_act = 8 # activity of remaining white matter
grey_matter_act = 16 # activity of remaining grey matter
```

REFERENCES

1. Wernick, M. N., and J. N. Aarsvold, *Emission Tomography, 1st Edition*, Chicago, USA: Elsevier, 2004. Available: https://shop.elsevier.com/books/emission-tomography/wernick/978-0-12-744482-6.

2. Ramon, A. J., Y. Yang, P. H. Pretorius, P. J. Slomka, and et al., "Investigation of dose reduction in cardiac perfusion spect via optimization and choice of the image reconstruction strategy," *Journal of Nuclear Cardiology*, Vol. 25, pp. 2117–2128, May 2017.

3. Noori-Asl, M., and A. Bitarafan-Rajabi, "Simulation and patient studies of scatter correction in cardiac spect imaging," *Iranian Journal of Medical Physics*, pp. 430-438, 2019.

4. Ogawa, K., Y. H. andTakashi Ichihara, A. Kubo, and S. Hashimoto, "A practical method for position-dependent compton-scatter correction in single photon emission ct," *IEEE TRANSACTIONS ON MEDICAL IMAGING*, Vol. 10, no. 3, pp. 408–412, 1991.

5. Ljungberg, M., ed., *Handbook of Nuclear Medicine and Molecular Imaging for Physicists: Instrumentation and Imaging Procedures, Volume I*, CRC Press, 2021.

6. Powsner, R. A., M. R. Palmer, and E. R. Powsner, *Essentials of Nuclear Medicine Physics and Instrumentation, 3rd Edition*, Wiley-Blackwell, 2013.

7. Segars, W. P., G. Sturgeon, S. Mendonca, and J. G. et al., "4d xcat phantom for multimodality imaging research," *IEEE Nuclear Science Symposium Conference Record*, Vol. 37, pp. 4902–4915, Aug 2010.

8. Hosny, T., M. M. Khalil, A. A. Elfiky1, and W. M. Elshemey, "Image quality characteristics of myocardial perfusion spect imaging using state-of-the-art commercial software algorithms: evaluation of 10 reconstruction methods," *American Journal of Nuclear Medicine and Molecular Imaging*, pp. 375–386, Dec 2020.

9. "Leading causes of death and disability 2000-2019: A visual summary.." Available at: https://www.who.int/data/stories/leading-causes-of-death-and-disability-2000-2019-a-visual-summary.

10. M. Lyra, A. P., M. Rouchota, and S. Synefia, "Filters in 2d and 3d cardiac spect image processing," *Cardiology Research and Practice*, Vol. 2014, pp. 1–11, Jan 2014.

11. Trevisan, A. C., M. D. Raed, V. Tumas, and L. A.-S. et al., "Comparison between osem and fbp reconstruction algorithms for the qualitative and quantitative interpretation of brain dat-spect using an anthropomorphic striatal phantom: implications for the practices," *Research on Biomedical Engineering*, Vol. 36, pp. 77–88, Jan 2020.

12. Yokoi, T., H. Shinohara, and H. Onishi, "Performance evaluation of osem reconstruction algorithm incorporating three-dimensional distance-dependent resolution compensation for brain spect: A simulation study," *Annals of Nuclear Medicine*, Vol. 16, pp. 11–18, Dec 2002.

13. Ljungberg, M., S.-E. Strand, and M. A. King, *Monte Carlo Calculations in Nuclear Medicine: Applications in Diagnostic Imaging*, CRC Press, 1998.

14. Okuda, K., K. Nakajima, M. Yamada, and H. W. et al., "Optimization of iterative reconstruction parameters with attenuation correction, scatter correction and resolution recovery in myocardial perfusion spect/ct," *Annals of Nuclear Medicine*, Vol. 28, pp. 60–68, Nov 2013.

15. Dheer, P., P. Gupta, S. Kamalakar, and T. et al., "Optimization of ordered subset expectation maximization parameters for image reconstruction in tc-99m methoxyisobutylisonitrile myocardial perfusion spect and comparison with corresponding filtered back projection-reconstructed images," *Indian Journal of Nuclear Medicine*, Vol. 36, Jan 2021.

16. de Barros, P. P., L. F. Metello, T. S. C. Camozzato, and D. M. da Silva Vieira, "Optimization of osem parameters in myocardial perfusion imaging reconstruction as a function of body mass index: a clinical approach," *Radiologia Brasileira*, Vol. 48, pp. 305–313, Oct 2015.

17. Dorbala, S., K. Ananthasubramaniam, I. S. Armstrong, and P. C. et al., "Single photon emission computed tomography (spect) myocardial perfusion imaging guidelines: Instrumentation, acquisition, processing, and interpretation," *Journal of Nuclear Cardiology*, Vol. 25, pp. 1784–1846, May 2018.

18. Boschi, A., L. Uccelli, L. Marvelli, and C. C. et al., "Technetium99m radiopharmaceuticals for ideal myocardial perfusion imaging: Lost and found opportunities," *Molecules*, Vol. 25, p. 1188, Feb 2022.

19. Hendel, R. C., D. S. Berman, S. J. Cullom, and W. F. et al., "Multicenter clinical trial to evaluate the efficacy of correction for photon attenuation and scatter in spect myocardial perfusion imaging," *Circulation*, pp. 2742–2749, 1999.

20. Khalil, M. M., *Basic Sciences of Nuclear Medicine*, Springer, 2010. Available: https://link.springer.com/book/10.1007/978-3-030-65245-6.

21. Jaszczak, R. J., K. L. Greer, C. E. Floyd, Jr., and C. C. H. et al., "Improved spect quantification using compensation for scattered photons," *Journal of Nuclear Medicine*, pp. 893–900, Aug 1984.

22. Can, M., O. Karadeniz, G. C. Kaya, and T. Ertay, "A study on energy window-based scatter correction methods in 99mtc and 123i imaging," *Journal of Instrumentation*, Vol. 18, no. 10, 2023.

23. "Xcat phantom program - cvit - center for virtual imaging trials," Oct 2022. Available at: https://cvit.duke.edu/resource/xcat-phantom-program/.

24. Segars, W. P., and B. M. W. Tsui, "Study of the efficacy of respiratory gating innmyocardial spect using the new 4d ncat phantom," *IEEE Nuclear Science Symposium Conference Record*, 2001. Available at: https://doi.org/10.1109/nssmic.2001.1008630.

25. "Simind manual pdf, lunds university." Available at: https://lu.app.box.com/s/o5jwq2j0blrm99ll5b1ld1e4d59tmisa.

26. Ejeh, J. E., J. A. V. Staden, and H. D. Raan, "Validation of simind monte carlo simulation software for modelling a siemens symbia t spect scintillation camera," *IFMBE proceedings*, pp. 573–576, 2018.

27. Domenico, G. D., S. D. Biaso, L. Longo, and A. T. et al., "Validation of simind monte carlo for 99mtc and 177lu," *Research Square*, Jul 2022.

28. Booyens, M., M. Morphis, J. Van Staden, and H. Du Raan, "Verification of a monte carlo simulated siemens symbia spect/ct," *European Journal of Medical Physics*, Vol. 31, Jul 2015. Available at: https://doi.org/10.1016/j.ejmp.2015.07.090.

29. "Symbia t series spect/ct, siemens healthineers usa." Available at: https://www.siemens-healthineers.com/en-us/molecular-imaging/spect-and-spect-ct/symbia-t.

30. "Selvamejia, infinia hawkeye 4 datasheet, scribd.." Available at: https://www.scribd.com/document/170635359/Infinia-Hawkeye4-Datasheet.

31. "Amide: a medical image data analysis tool." Available at: https://amide.sourceforge.net/.

32. Rahimian, A., M. Etehadtavakol, M. Moslehi, and E. Y. K. Ng, "Myocardial perfusion single-photon emission computed tomography (spect) image denoising: A comparative study," *Diagnostics (Basel)*, Vol. 13, p. 611, Feb 2023.

33. Kortelainen, M. J., T. M. Koivumaki, M. J. Vauhkonen, and M. A. Hakulinen, "Dependence of left ventricular functional parameters on image acquisition time in cardiac-gated myocardial perfusion spect," *Journal of Nuclear Cardiology*, Vol. 22, pp. 643–651, Aug 2015.

34. Tantawy, H. M., Y. G. Abdelhafez, N. L. Helal, and I. E. Saad, "Variation of contrast values for myocardial perfusion imaging in singlephoton emission computed tomography/computed tomography hybrid systems with different correction methods," *Journal of Clinical Imaging Science*, Vol. 25, p. 1188, Feb 2020. Available at: https://doi.org/10.25259/jcis_123_2020.